UWB Air-Coupled Antenna for Ground Penetrating Radar

Thesis submitted for the degree of
Master of Science in Electrical Engineering

Hossein Azodi

Supervisor:
prof.dr.sci. A. Yarovoy

Daily Supervisor:
ir. X. Zhuge

2009-2010

TU Delft

Faculty of Electrical Engineering, Mathematics and Computer Science

Delft University of Technology

UWB Air-Coupled Antenna for Ground Penetrating Radar

Thesis

submitted in partial fulfillment of the
requirements for the degree of

Master of Science

in

Electrical Engineering

by

Hossein Azodi
born in Tehran, Iran

This work is performed at:

Microwave Technology & Systems for Radar Section
Department of Telecommunications
Faculty of Electrical Engineering, Mathematics and Computer Science
Delft University of Technology

Delft University of Technology

Delft University of Technology
Department of
Telecommunications

The undersigned, hereby, certify that they have read and recommend to the Faculty of Electrical Engineering, Mathematics and Computer Science for acceptance a thesis entitled **"UWB Air-Coupled Antenna for Ground Penetrating Radar"** by **Hossein Azodi** in partial fulfillment of the requirements for the degree of **Master of Science**.

Dated: September 16, 2010

Chairman:

prof.dr.sci. A.G. Yarovyi

Advisor:

ir. X. Zhuge

Committee Members:

prof.dr. A. Neto

dr.ir. B.J. Kooij

Abstract

Ground Penetrating Radar (GPR) is a promising technology to detect buried objects beneath or near ground surface. To achieve high-resolution and accurate enough images, the transmitting antenna (TX) in this technology is required to radiate a highly-correlated narrow width pulse towards ground where the targets are hidden.

For this application, an ultra-wide bandwidth ($0.3-6$ GHz) antenna from the family of Vivaldi antennas is designed and optimized. This antenna meets the required features of the TX antenna both in frequency and time domains. Apart from its broadband characteristics, the antenna radiates highly correlated pulse towards its footprint. It, also, shows very low late-time ringing and has narrow width impulse response. The antenna is designed on $\epsilon_r = 2.33$ dielectric substrate and is fed via a 50 Ω SMA end-launch.

Acknowledgments

Hereby, I would like to express my sincere gratitude to my supervisor, prof.dr.sci. Alexander Yarovoy. His immense knowledge and enormous experience in the field of Applied Electromagnetic was the asset without which my Thesis would not have been possible. It is my great pleasure that not only I could learn technical, but also ethical and social lessons from his guidance and advice. I would like to thank him again to-the-most for his supports which encouraged me to reach the ultimate goals of the Thesis. Then, deep and warm thanks to my daily supervisor, ir. Xiaodong Zhuge, who patiently listened to me, helped and closely supervised me throughout this project. His always-available schedule, in the busy hours PhD candidates have, was priceless for me.

I also extend my gratitude to Denny Tran, dr. Massimiliano Simeoni and ir. Bill Yang who supported me to solve many practical and theoretical problems. I would like to thank my nice colleagues Wyger Brink, Pablo Rodriguez Ulibarri and Mark Apeldoorn as well for the fruitful atmosphere and enjoyable working hours we have had. Additionally, the special thanks to one of my best friends, Ali Rostamzad Mansour, who aesthetically designed the cover page of this Thesis report.

Above all, I would like to express my deepest love to my parents, Fariba and Hamid, who encouraged and supported me throughout each step of my life and specially during my master study and my young sister, Setareh, who I incredibly missed over these days in the Netherlands.

Last but not least, thanks Leila for all the unforgettable moments we have shared and for tasting me the new melodious shape of life.

Hossein Azodi

September 16, 2010

Contents

List of Figures

1 Introduction

In this chapter, a general overview of the Thesis is given. In the first section, ground penetrating radars are briefly described. In section 1.2, the main problem of the Thesis as well as the ultimate objectives are explained. Section 1.3 points to a review on the mostly current ultra wide band (UWB) antennas. Introducing these antennas which are standing on the state-of-the-art, novelties of the Thesis and the approach to solve the problem are addressed in section 1.4. Finally, the outline of the Thesis is mentioned in section 1.5.

1.1 Ground Penetrating Radars

Ground penetrating radars (GPR) are a group of subsurface and/or near-surface radars intended to detect buried objects remotely. Among all other technologies to detect objects hidden by an optically opaque surface, GPR is developed and showed a promising performance over the past few decades. Designing a GPR system, in general, is challenging and complicated. The complexity is mainly due to various fields of research such as electromagnetic wave propagation in lossy media, UWB antenna design, and signal processing which are incorporated in this technology [2].

Most of GPR systems are funded based on impulse radar technology. In this technology the transmitting (TX) antenna sends an impulse to ground surface under where the targets are hidden. This electromagnetic wave can

efficiently penetrate the surface if it is coupled to ground. Thus, it is one of the main intentions of many antenna designers to couple the TX antenna and the ground.

The target reflects and scatters the radiated electromagnetic impulse, based on the dielectric discontinuities with the soil. Then, the receiving antennas (RX) collect the back-scattered signal partially. This back-scattered signal will be extracted by signal and image processing techniques to visualize the target in an user-friendly manner. So, in parallel to this field of research, improvements in signal and image processing techniques help realizing the idea of fast-recovery high-resolution GPR, eventually.

The targets might be located at any depth beneath the ground surface depends on the particular application. The detection depth, as an important feature, relies on the low frequency components of the radiated pulse due to the fact that these components penetrate more inside the soil. Higher frequency components, on the other hand, increase the resolution. Hence, the desired resolution can be obtained if a sufficient bandwidth is chosen.

Over the years, GPR has been shown as an UWB system which is more challenging than ordinary radar systems due to the higher clutter-to-signal ratios [2]. Recently developed GPR systems have higher speed, higher resolution and cheaper prices. Research in this direction mainly focuses on obtaining a fast recovery accurate-enough images from buried objects, indeed [3], [4].

Applications of GPR are in a vast group from commercially ones such as utility pipes and cables detection, to military ones such as anti-personnel and anti-tank land-mines detection, to archaeological investigations, to Geophysical investigations, to oil and gas explorations and so forth [1].Apart from

[1]A more complete list of applications can be found in [2]

the direct applications and benefits, the investigation in this vibrant field of research can be applied to and helps maturing other radar technologies such as medical imaging and through-wall detection, and vice versa, thanks to the similarity between the inverse scattering problem they all are dealing with.

1.2 Research Problem Description and Objectives

In-line with ongoing research over this sophisticated developing radar system, Microwave Technology and Systems for Radar Section of Department of Electrical Engineering, Mathematics, and Computer Engineering (EEMCS) at Delft University of Technology (TU Delft) has focused on this particular field of research for more than a decade. The experimental developed GPR system for this purpose is depicted in figure 1.1. A single TX antenna is illustrated in the middle of the figure. Also, one might find a linear array of RX antennas located underneath TX antenna near the ground. The initial system is working with the dielectric wedge antenna [5] as the single TX antenna and loop antenna as elements of RX array. This GPR system is intended to detect buried land mines and utility pipes or cables.

As explained earlier in this chapter, an ultra short pulse derives the TX antenna and a reflected pulse from the target will be captured by RX antennas. Figure 1.2 illustrates a sample deriving pulse as well as the radiated pulse somewhere on the ground. The main objective of the Thesis is to design (or improve) the high performance TX antenna for this GPR system such that the radiated impulse on the ground correlates to the deriving pulse highly and without late time ringing. In reality, higher than 95% correlation and less than -20dB with respect to the highest peak-to-peak

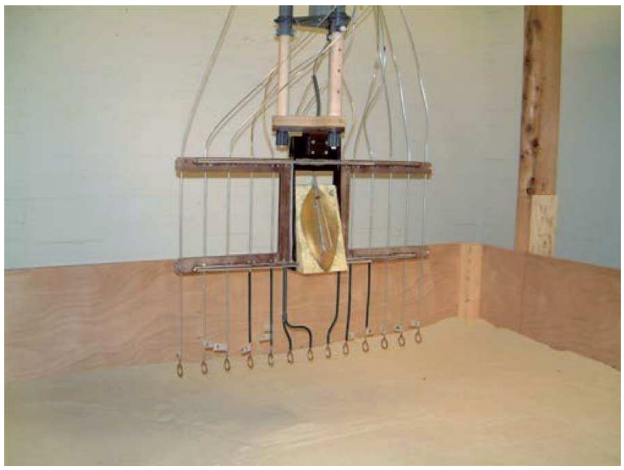

Figure 1.1: GPR system at TU Delft

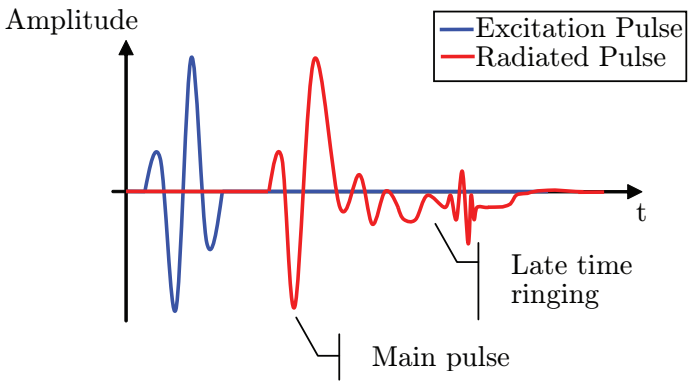

Figure 1.2: Schematic of the Excitation and Radiated Pulses

value of the pulse are the acceptable measures for this GPR. Also, the operating frequency range of the antenna should be specified. Due to the fact that the depth of targets are a few meters, the low frequency should be at least 300 MHz. On the other side, resolution of the radar is guaranteed by ultra wide frequency bandwidth of the TX pulse. To meet the depth and the resolution requirements concurrently, the antenna should operate from 0.3 to 6 GHz. This means the return loss in this frequency band should be lower than -10 dB.

Apart from these strictly defined features, there are a few features that the antenna should posses. These are not quantized i.e., it is better to have an antenna with these qualities than without them. For example, to radiate one narrow pulse towards the ground, the TX antenna should not distort the deriving pulse. Thus, it is better if the antenna radiates different frequency components of the pulse almost in the same spot i.e., it should have a fixed phase center.

Furthermore, it is preferable that the TX antenna has a stable and flat gain as well as constant group delay. The former is important to assure that the radiated pulses have the same peak-to-peak level on the ground. Hence, the reflected pulses from the ground would not have been affected by the variation of the antenna gain instead of the contrast in permittivities. The latter is, also, important to keep the pulse width as narrow as the deriving pulse.

Another feature, the TX antenna should better posses, is the linear polarization of the transmitted pulse. Low cross-polarization should be taken into account in order to obtain more accurate information regarding the direction and the shape of the target.

Last but not least, the antenna should be feasible to manufacture with respect to the dimensions and the materials which are used in the design of the antenna.

1.3 State-of-the-Art in UWB Antenna Design

UWB antennas are designed not only for radar applications, but also for telecommunications for decades. There are, surely, other novel UWB antennas proposed and designed, which are not covered in this section. Nonethe-

less, the discussed antennas are a group of current antennas for the radar applications due to the scope of the Thesis.

Resistively loaded dipoles and monopoles are a group of antennas which are used for GPR applications [2]. In a recent work, a resistively loaded antenna with higher-efficiency and more accurate modeling has been designed specifically for GPR applications [6]. This antenna operates over the frequency band of 275 to 475 MHz. Another type in this group is the resistively loaded vee-dipole. In [7], a $6:1$ UWB antenna has been designed using well-known Wu-King profile.

Bow-tie antenna is another group of antennas which is conventionally known as the planar form of the bi-cone antenna. This group of antennas, in recent years, are combined with various resistive loading to increase the bandwidth and decrease the late-time ringing phenomenon which happens because of reflections from the edges of the antenna. In [4], a bow-tie antenna with the bandwidth of $0.495 - 5.155$ GHz has been designed. In continuation to this work, in [8], a wire bow-tie antenna has been designed and experimentally verified with an 0.8 ns pulse. The main advantage of this antenna over the previous versions is the fact that using the flare angle, this antenna can be adapted for various ground types based on their electromagnetic characterization.

In addition to previous groups, recently, there are many efforts to develop Vivaldi antennas for various radar applications, including GPR [9], [10], [11]. These are just a few of dozens of papers published recently in journals and conferences in which a type of Vivaldi antenna has been proposed. In [12], corrugation of the ending is used as a technique to increase the performance of the antenna by killing the back-ward currents in the flares. This approach was hardly successful, though. In another approach [13], circularly ended

Vivaldi antenna has been designed and experimentally verified. The antenna operates in the bandwidth of 2.6 to 27 GHz with a highly efficient pulse emission towards the end-fire direction.

1.4 Research Approach and Novelties

In order to obtain the ultimate goals of this project, almost all of the conventional UWB antennas have been studied, first. The study shows that the Vivaldi antenna is capable of fulfilling the required features of this project. In the next step, the choice of balanced antipodal Vivaldi antenna (BAVA) has been approved among other types of Vivaldi by the result of different simulations.

In the main portion of the work, the BAVA has been optimized based on the required features. Optimization of the antenna is started on the flares to achieve the designated return loss. Then, the matching and transition sections have been optimized to obtain the required characteristics in frequency domain, such as constant group delay and lower than -16 dB return loss in the line. The main novelty of the work is the modification of the transition section between the transmission line and the flares of the antenna. With this new transition section, the operating frequency band from 0.3 to 6 GHz corresponding to $20:1$ bandwidth ratio has been achieved.

In the design of this antenna real and practical scenarios are considered to prepare the antenna for manufacturing process and experimental verification. Thus, matching to 50 Ω impedance with real materials was one of the main considerations. In order to realize the proposed antenna, it is designed on *Rogers RT/duroid 5870* with $\epsilon_r = 2.33$ and connected to the 50 Ω coaxial-cable by Emerson Networks SMA - 50 Ω end-launch jack re-

ceptacle. Sufficient room for soldering the end-launch on the antenna has been provided, indeed.

As a summary, the objectives of the Thesis are attained by designing an UWB antenna for GPR. The simulations, by considering the real scenarios, approves the capabilities of the antenna. At the end, it can be manufactured and experimentally verified.

1.5 Thesis Organization

In Chapter 2, various UWB antennas are discussed with respect to their designs, layouts and radiation characteristics. Based on this study, the optimum antenna structure is chosen i.e., the Vivaldi antennas. Then, the simulation results are presented to confirm the capability of balanced antipodal Vivaldi antenna among other Vivaldi antennas.

Chapter 3 covers the entire process of design and optimization of the BAVA antenna. The sections of this chapter reflect the steps in designing the proposed BAVA based on the desired features. The novelty of the design is also explained in this chapter. At the end, results of the simulations will be provided. The focus in this chapter is on return loss of the antenna to get the required bandwidth.

In Chapter 4, the ending of the antenna is investigated. Moreover, the SMA connector is included in all simulations to complete the model of the antenna. Simulation results of the optimum BAVA design are illustrated. Then, the radiation characteristics of the finalized antenna layout are discussed.

Finally, Chapter 5, concludes the report. Also, the future works, suggestions and recommendations are mentioned in this chapter.

2 UWB Antenna Candidates

In this chapter, the appropriate antenna structure for the rest of the project is introduced. In order to find this candidate, in the first step, characteristics of various UWB antennas are studied to the details. A family of antennas is selected which match closely to the required characteristics mentioned in chapter 1. Finding the potential candidates, different aspects of them have been tested by simulations. The results of these simulations are explained in section 2.2. These results confirm the capabilities of the suggested structure. Finally, the antenna structure has been selected based on the studied literature and the simulations.

2.1 Study of UWB Antennas

The result of the study on various UWB antennas is briefly explained in this section. These antennas are gathered from different families of UWB antennas. Within each family, there might be various layouts, types, structures, modifications, etc. Nonetheless, an overview of the radiation mechanism is drawn with respect to the scope of the Thesis.

2.1.1 Horn Antenna

Horn antenna is one the oldest antennas in Telecommunication Engineering [1]. Its promising broadband operating frequency - commercially $1-11$ GHz - has made this antenna one of the best candidates for short-pulse commu-

nications as well as radar applications for many years. This antenna has linear polarization and directive pattern which both are convenient for the purpose of this work.

Ridged horn antenna has the same structure as the conventional horn antenna, except that it has metallic ridges on flared sections of the waveguide. In this way, the antenna operates over larger frequency band, e.g., $1 - 18$ GHz [14]. A sample ridged horn antenna is shown in figure 2.1.

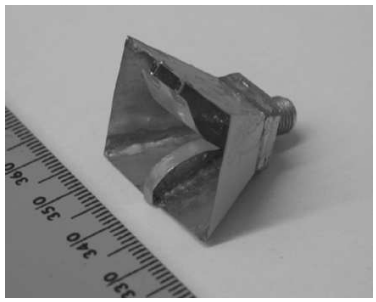

Figure 2.1: Ridged Horn Antenna. This is taken from [1].

Wedge antenna works based on the same mechanism as the horn antenna. In a recent work, the shape of flares of this antenna is modified [5]. This antenna is, also, loaded with an specific dielectric, very similar to other dielectric loaded horn antennas [15]. This type of the antenna, eventually, has less ringing and better matching to the ground by paying the cost of radiation efficiency.

Despite all of the advantages in far-field, horn antenna is not capable of working near the ground. Qualitatively, the radiated pulse from the horn antenna bounces back to the antenna flares while it is working near the ground. The bounced pulse will be radiated back by the antenna flares towards the ground again. This effect might happen several times which at the end leads to multiple reflection and late-time ringing. Moreover, the

horn antenna is bulky in comparison to planar antennas. It is, also, costly to manufacture.

2.1.2 Bow-tie Antenna

Bow-tie antenna, as illustrated in figure 2.2, is the planar form of bi-conical antenna. This type of antenna has been used in different applications, specifically for impulse radio and GPR [16], [17]. Bow-tie antenna has dipole-like pattern and the radiated wave from this antenna is linearly polarization. Typical gain of bow-tie antenna is $5-6$ dBi which is higher than normal dipole antennas. Additionally, it can work over wider frequency band in comparison with dipole or resistively loaded dipole antennas [15].

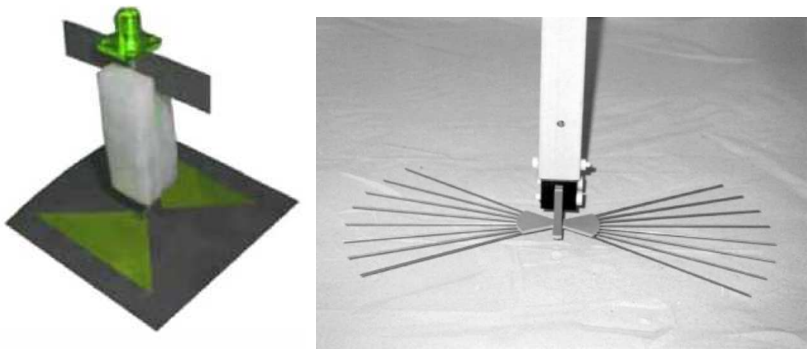

(a) fed symmetrically in the center

(b) wire realization

Figure 2.2: Two Types of Bow-tie Antenna

Over the years, different modifications have been applied to this antenna to make it more suitable for the TX antenna of GPR. The bow-tie antenna can be improved to operate over wider bandwidths by applying resistive loading [4], [16] and [18]. In [4], instead of just a resistive loading profile a resistive-capacitive loading profile is proposed. It is also ended by a circu-

lar curve which helps alleviating the late-time ringing phenomenon in the radiated pulse. This antenna, finally, shows a stable radiation pattern until 3.5 GHz and then breaks down.

Apart from the ordinary designs, the concept of "adaptiveness" with respect to various soil types has been realized in [3]. This is an important feature when the GPR is intended to be used for different soil types with different electrical characteristics. The idea of adaptation is implemented by controlling the flare angle so that the antenna can be coupled to ground. In [8], this idea has been realized with a wire bow-tie antenna. Figure 2.2(b) shows this antenna.

Another type of bow-tie antenna is, namely, aperture coupled bow-tie antenna [19]. Type of feeding is the difference between this antenna and the previously introduced bow-tie antennas. This antenna is fed by a broadband stub. A recent design of aperture coupled bow-tie antenna can be found in [20]. This antenna is printed on a rectangular patch and works in FCC UWB range for communication with an almost constant group delay.

In contrary to the advantages of bow-tie antenna such as simple design, it does not exhibit a broadband characteristics [21]. That is why different resistive methods have been used so far to incorporate the broadband characteristics in this antenna. Additionally, bow-tie has an omni-directional radiation pattern instead of directional radiation pattern which is necessary for GPR applications.

2.1.3 Monopole Antenna

Monocone antenna is a type of monopole antenna mounted on a ground plate. Monocone antenna has linear polarization and omni-directional ra-

diation pattern. The antenna can emit UWB if the size of ground plane is infinite [19]. Reducing the plane size in practical cases, the bandwidth of the antenna degrades.

One of the main disadvantages is the difficulty of matching the antenna to 50 Ω impedance of feeding when the size of the ground is reduced. Recently, an UWB inverted-hat monopole antenna has been designed which is suitable for applications in the range of 50 MHz $-$ 2 GHz. For operating in this frequency band, it has reasonable dimensions [22]. This antenna shows promising matching to the 50 Ω impedance, however, its omni-directional radiation pattern is not suitable for radar applications. Also, the three-dimensional structure of this antenna has made it bulky for our specific application.

The planar form of the monopole antenna is designed to solve the bulkiness structure of this antenna. Thanks to the advances in Printed Circuit Board (PCB) technology, it can be manufactured simply and it would be inexpensive. The antenna characteristics are mainly inherited from the monopole antennas e.g., omni-directional pattern, breaking-down effect in high-frequencies, etc. Typical average gain for this type of antennas is $6-7$ dBi which is higher than monocone antennas with $4-5$ dBi.

2.1.4 Spiral Antenna

Spiral[1] antenna is a type of self-complementary antennas. No matter which category is used, the invariant input impedance is an attractive feature for many antenna engineers [19]. In theory, the input impedance of this antenna should be 164 Ω [21], but finite length, finite thickness and non-ideal feeding

[1]This antenna has three sub-categories: the logarithmic (or equiangular), Archimedian (or arithmetic) and rectangular. The spiral antenna is used to address the first type which is more common.

condition cause variation of this number. Typically, the input impedance of these types of antennas are between $150-200\ \Omega$ [23] over their operating frequency band. The wave, when fed to the antenna, is radiated and vanishes on the legs of the spiral antenna. The higher frequencies are radiated first and lower frequency components later [24]. This effect i.e., dependency of radiation spot to the frequency, is the main reason why this antenna dispersively radiate the pulse and is not suitable for our purpose.

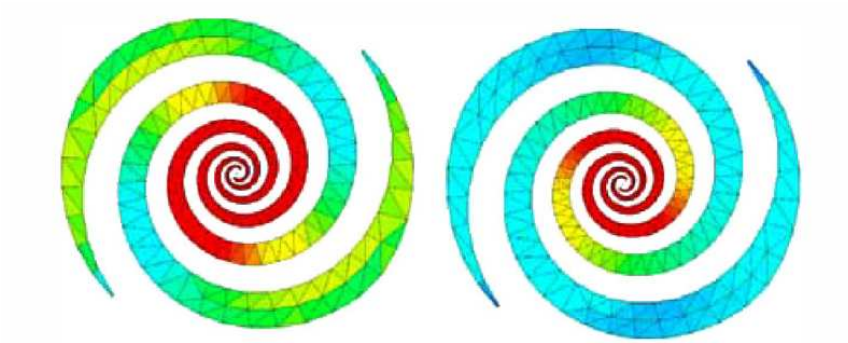

Figure 2.3: Current Distribution on Spiral Antenna at 300 MHz (left) and 450 MHz (right)

On the other hand, based on the radiation mechanism of the spiral antenna, the radiated wave has circular polarization and its phase center is distributed [25]. These issues made this antenna not-suitable for GPR applications. Specifically, the latter can be seen in figure 2.3[2] which shows the current distribution on a logarithmic spiral antenna at 300 and 450 MHz.

2.1.5 Vivaldi Antenna

The Vivaldi antenna was first introduced by Gibson in "The Vivaldi aerial" [26]. Since then, it is widely used in different applications such as microwave imaging, wireless communications and ground penetrating radars [19]. The

[2]This picture is directly taken from [19]

Vivaldi antenna, nowadays, has three main categories: The coplanar Vivaldi antenna which is introduced by Gibson [26], the antipodal Vivaldi antenna [27] and balanced antipodal Vivaldi antenna [28]. These categories, in general, have the exponentially tapered flares in common. In all of them, traveling wave on the inner edges of the flares is the main mechanism for radiation. So, exponentially tapered flare is the unique quality which makes the antenna operates over a broad frequency band [29]. Similar to bow-tie antenna, Vivaldi antenna can be manufactured reasonably cheap using PCB technology.

In coplanar Vivaldi antenna, the oldest form of Vivaldi, two radiator planes are on the same side of the dielectric sheet. This structure has been shown in figure 2.4(a). The antenna can be fed by aperture coupling from the other side as depicted in this figure. A recent sample of this type of feeding can be found in [30]. There is another feeding circuit using broadband balun which is not convenient in many designs due to the length of these baluns and the complexity they might add to the structure [31].

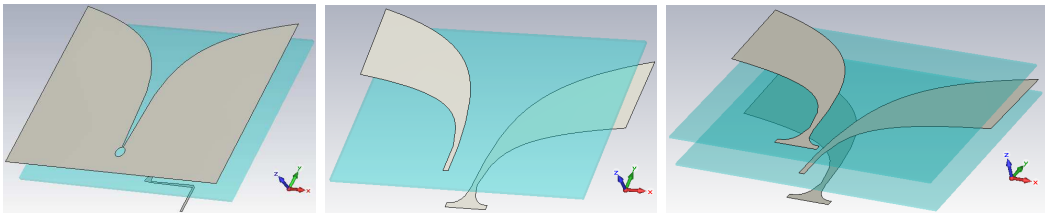

(a) Coplanar (b) Antipodal (c) Balanced Antipodal

Figure 2.4: Three Structures of the Vivaldi Antenna

The antipodal Vivaldi antenna (figure 2.4(b)) is proposed to solve the feeding in coplanar ones. In this type of Vivaldi antenna one of the layers is printed on top and the other one which is tapered in opposite direction

is printed on the bottom of the dielectric substrate sheet. This antenna can be fed easily by soldering the connector to the two sides of the sheet. The matching to conventional 50 Ω lines is easier thanks to the transition between twin parallel stripline to microstrip line [9], [11], [13]. The antipodal Vivaldi antenna, however, increase the cross-polarized radiation which is not suitable for radar applications. This can be improved by balanced antipodal structure of Vivaldi antenna, figure 2.4(c).

In balanced antipodal Vivaldi antenna, another dielectric sheet has been added on top of the antipodal structure and a metal plate just like the one in the bottom of the antenna has been printed on top of the newly added sheet.

One modification to antipodal Vivaldi antenna is to resistively load the antenna. The loading profiles are mainly used to decrease the reflection from the opening (end) of the antenna which causes late-time radiation (ringing) and ripples in the gain which are both undesirable in UWB applications [11]. The resistive loading is added where the currents are moving backward to the excitation port. In this way, they were killed before they are reflected back in the antenna.

Almost flat gain in the entire bandwidth, low cross-polarization and high directivity can also be mentioned as other advantages of all Vivaldi antennas [9], [13]. Moreover, the time-domain characteristics of this antenna shows promising capabilities regarding the radiation of the same pulse over the entire area of illumination i.e., footprint [30], [32]. In [13], the proposed antenna shows almost constant group delay in the entire band which is very important to have a non-distorted radiated signal.

Based on the characteristics which have been studied in the available literature, it becomes evident that the Vivaldi antenna is a good candidate

for the purpose of this project. This antenna can possibly fulfill all requirements of the design specification. To see which type of the Vivaldi is more suitable for our purpose, a comparative study has been done between the three structures of Vivaldi antenna. The result of the simulation and the final choice for the rest of this project is elucidated in the next section of this chapter.

2.2 Comparative Study of Vivaldi Structures

In this section, three structures of Vivaldi antenna are compared on various aspects of radiation characteristics. It should be noted that the sample antennas (models) in this section are not optimized, but the results at the end are valid enough to make the final choice for the rest of this project. This decision is, actually, valid because for each structure, 3 models are designed. So, in total 9 antennas are compared. For each structure, the quasi-optimum model is used for comparison. This can guarantee that even though the antennas are not optimized, the result of the quasi-optimum model in each criterion demonstrates the capability of that structure. In other words, the quasi-optimum model is the representative of its structure for each criterion.

Also, the matching section of the antenna is excluded from the structures so that the result of experiments are comparable and, more importantly, they are independent from the matching properties of the structure. The same waveguide port in CST Microwave Studio is directly [3] connected and matched to the antenna radiating flares. So, the simulations only depend

[3]It should be noted that a small microstrip line ($\lambda_{min}/3$) has been added to the each model, otherwise the software would not be able to commence the simulations due to the shortness error of the waveguide.

on the radiating characteristics of the antenna and not on the matching section. The matching section can be easily optimized in the future if the correct structure would have been chosen.

2.2.1 Simulation Results of Vivaldi models

For each structure of the Vivaldi antenna as mentioned earlier, three models are investigated. This is only to increase the accuracy of the final decision and decrease its dependency on models. Instead, the dependency will be more on structure of the antenna. The idea is that by comparing three models for each structure the quasi-optimized results might be obtained which are sufficiently valid for this purpose.

In figure 2.5(a), the curves which are used to create models of the coplanar structure are illustrated and, in figure 2.5(b), the same has been illustrated for antipodal and balanced antipodal structures. The curves in figure 2.5 are based on exponential relationship between x and y with different constants. These curves cover a wide range from the sharpest to smoothest exponential curves between the same start and end points on the plane which again provide the better overview of each structure.

The best return loss among the models of each structure is depicted in figure 2.6. The criteria for choosing the representative i.e., quasi optimum, of each structure, in this respect, are wider bandwidth due to the definition of $S_{11} \leq -10$ dB and less number of peaks. The return loss graphs of the quasi-optimum models, thus, show that the coplanar structure has lots of resonances. This can be figured out from the enormous number of peaks in the return loss of this model. This characteristic is not convenient for UWB antenna because the radiated pulse of such antennas is a distorted version

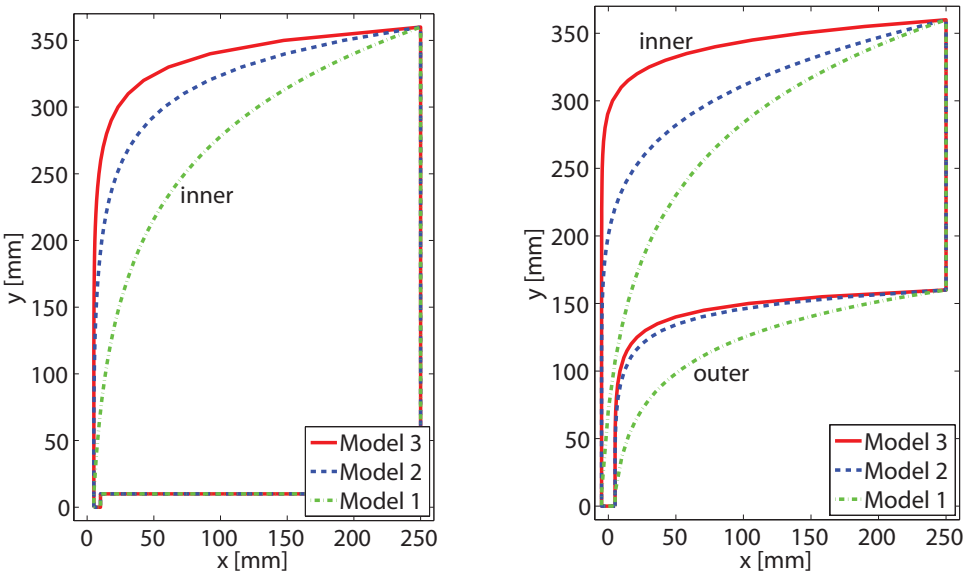

(a) Coplanar (b) Antipodal and Balanced Antipodal

Figure 2.5: Curves of 3 Models for Each Structure

of their excitation pulse with wider time-width. Even though that the coplanar antenna has wider operational bandwidth with respect to -10 dB criterion, it does not show suitable frequency-domain characteristic as an UWB radiator.

Antipodal representative in this experiment shows wider frequency bandwidth than the balanced antipodal counter-part. However, in higher frequencies, the balanced antipodal antenna performs even better than antipodal structure with lower return loss levels i.e., higher matching levels. Additionally, the balanced antipodal model shows less number of resonances in its structure which is obvious in figure 2.6 by considering the number of peaks in the return loss of the antipodal and balanced antipodal representatives. This means that the wave on the balanced antipodal can better

travel and less reflected within the antenna structure than the others.

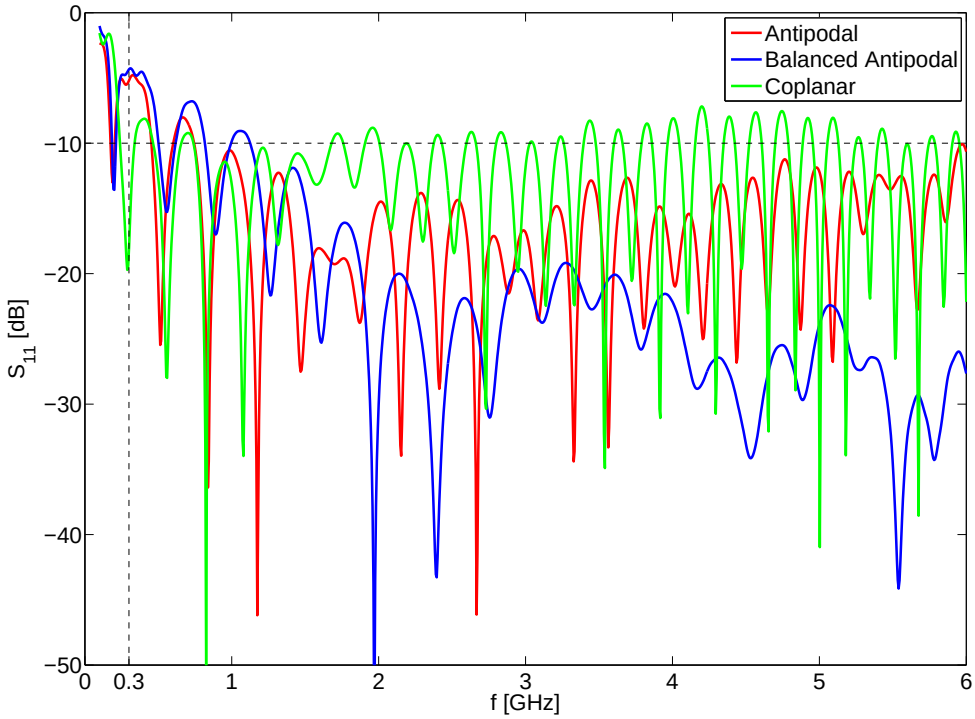

Figure 2.6: Return Loss of the Quasi-optimum Model of Each Structure

In addition to return loss result, the best far-field pattern of electrical field in E-plane for each structure is depicted in figure 2.7. The criteria of choosing the representative of each structure are the gain and the stability over different frequencies. So, the model 1, for instance, is chosen as quasi-optimum for antipodal and balanced antipodal while the model 2 is found optimum within coplanar models. This is just one example where one curve shows better results for one specific structure and this is exactly the main reason to extend the number of models from 1 to 3, based on different curves.

Figure 2.7 has a very clear message. It shows that the balanced antipodal representative model has very stable, and flat pattern over the operating frequency band. It also shows that the back-radiation - another unwanted

characteristic of the directional antennas - is lower for balanced antipodal in comparison to others. Lower sidelobes' levels of this model in comparison to others can be seen in this figure as well. The gain of balanced antipodal model is also higher than its counter-parts over all sampled frequencies. It should be noted that these models, as depicted in figure 2.6, are more reflecting the signal than radiating it in frequencies lower than 2 GHz. Thus, the pattern is not valid for comparison in lower frequencies.

The similar results are obtained in H-plane. Figure 2.8 shows the pattern of the quasi-optimum models of each structure at $f = 3.5$ GHz. This figure proves that the balanced antipodal antenna has a flat and higher gain in the end-fire direction, and less side- and back-lobes' levels. The H-plane patterns in other frequencies are also confirming the obtained result at $f = 3.5$ GHz. So, they are skipped without loosing any generality.

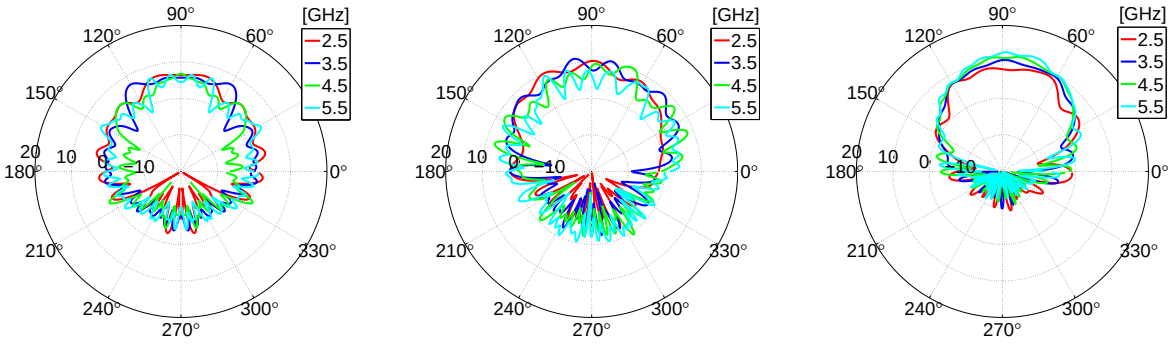

(a) Coplanar (b) Antipodal (c) Balanced Antipodal

Figure 2.7: Far-field E-plane Pattern of the Quasi-optimum Model of Each Structure at Different Frequencies

Another aspect for comparing the three structures is to look at their radiated pulse. This has been done by adding two far-field probes in the plane of the antenna ($xy-$plane) far from the antenna on the end-fire axis

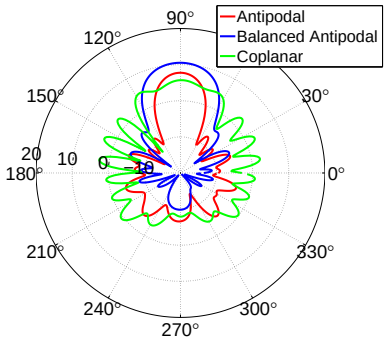

Figure 2.8: Far-field H-plane Pattern of the Quasi-optimum Model of Each Structure at $f = 3.5$ GHz

- $y-$axis - of the antenna and in co- and cross-polar configurations, i.e., in $\hat{x}$ and $\hat{z}$ directions, respectively. The best result of each structure in this experiment has been depicted in figure 2.9.

In figure 2.9(a), captured pulse of co-polar probes has been illustrated. This figure shows that there are 3 time-slot in which the radiation have been occurred. The first ringing occurs in the range of $5.7 < t < 6.7$ ns. This is the main radiation of the models. In this range, radiated pulse of the balanced antipodal model has narrower width and higher peak-to-peak level. The second ringing happens just afterwards. In this range, which is an inconvenient ringing, the balanced antipodal has only one peak. Its radiated pulse, thus, has narrower width while the width is increased due to multiple radiations in antipodal and coplanar structures in this range.

The third ringing occurs in the range of $8.1 < t < 9.6$ ns. This is late-time ringing of the antennas in which again balanced antipodal performs better by less peak-to-peak levels. Coplanar model is the worst in this sense with lowest peak-to-peak level and higher late-time ringings. It, also, distorts the excitation pulse as expected based on the return loss and pattern of this antenna structure. The peak-to-peak levels and late-time ringing of

the antipodal model can be optimized, as seen in the literature, to meet the requirements of this project. However, the coplanar model has so many resonances in the structure such that the optimization seems to be extremely difficult, if not impossible.

Figure 2.9(b) illustrates the cross-polar radiated pulse of the quasi-optimum model of each structure. As expected, the coplanar model has the lowest peak-to-peak levels. The balanced antipodal model has slightly low peak-to-peak levels in this respect. The worst model in this aspect is the antipodal structure.

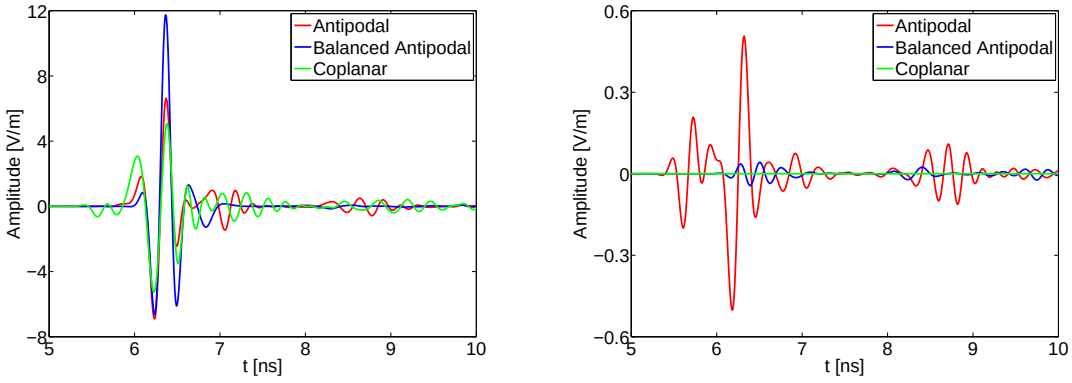

(a) Co-polar Probe

(b) Cross-polar Probe

Figure 2.9: Radiated Far-field Pulse of Quasi-optimum Models in End-fire Direction

The source of this cross-polar radiated fields can be found by checking the cross-section of the antennas. The antipodal antenna has 2 metal layers on 2 sides of the dielectric substrate. The Electric fields, as the result, has a non-zero component orthogonal to the co-polar reference of the antenna. This component has been canceled by adding another metallic layer in the balanced antipodal antenna and that is the reason why the cross-polar radiation in this direction is degraded for balanced antipodal Vivaldi antenna.

The coplanar Vivaldi antenna, in this respect, does not have any field in cross-polar reference which can be also confirmed by checking figure 2.9(b) where the cross-pol radiated field of the coplanar Vivaldi antenna is almost zero.

There is another source of cross-polar radiation in the Vivaldi antenna and similar exponentially planar tapered antennas, in spite of common sense [33]. This source is mainly the currents which are circulating at the opening end of the antenna. This effect can be seen by probes which are not in the same plane of the antenna, but in upper or lower planes. It is studied and reported in this Thesis later in this chapter.

In order to visualize the radiated pulse in near field of the antenna, another experiment has been done. In this experiment, 101 equidistant co-polar probes are located in the E-plane of the antenna on a straight line. The line is located along the $x-$ axis and 30 cm above the end of the antenna, as depicted in figure 2.10. Again, quasi-optimum results are considered and they are depicted as B-scan plots in figure 2.11. These plots show the radiated pulse with respect to the location of the probes and time. The color-bar in the figure indicates the amplitude of the pulse. This is the efficient way of looking at late-time ringing of these models.

From figure 2.11, it can be seen that this phenomenon is more severe in coplanar model. The figure, also, shows that the balanced antipodal model has slightly lower late-time ringing. The same experiment has been done for co-polar probes in H-plane of the models. The quasi-optimum results approve that the balanced antipodal model has less ringing after its main radiated pulse.

Moreover, the width of the radiated pulse can be measured in time axis of these figures. In this respect, balanced antipodal has the short-

est width while antipodal has slightly larger width and coplanar Vivaldi antenna ranked in the last position.

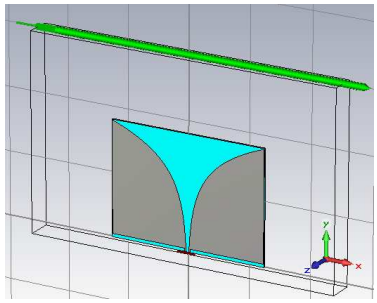

Figure 2.10: Configuration of the Probes in E-plane for Near-field Radiated Pulse

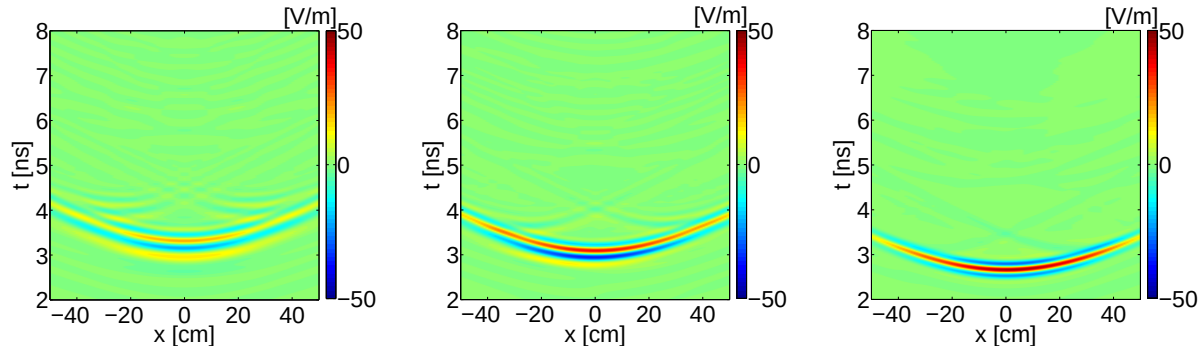

(a) Coplanar (b) Antipodal (c) Balanced Antipodal

Figure 2.11: B-scan of Radiated Near-field Pulse of Quasi-optimum Models in E-plane

2.2.2 Choosing the Structure

Based on the simulation results as well as literature study, the evidents and proofs are enough for concluding that the balanced antipodal Vivaldi antenna can fulfill the requirements of our project. This antenna has less resonances in its structure which can be seen in its smoother S_{11} over the operating frequency band. It, also, shows more stable pattern in differ-

ent frequencies with lower back- and side-lobes' levels. The radiated pulse of this antenna is high-enough correlated to the derivative of the original pulse over a wide angle on the ground and it shows very small late-time radiation which can be, again, reduced by optimization of the antenna. It has higher gain and efficiency than the other structures. Last but not least, balanced antipodal Vivaldi antenna reaches a certain level of matching with substrate's permittivity below 2.5 where there are plenty of materials available in the market, while antipodal and coplanar reach the same level with higher than 3 and 6, respectively.

On the other side, this antenna seems to be more difficult to feed because of its geometry. Actually, the inner metal layer which should be connected to the pin of the coaxial cable is hidden between to substrate sheets. This issue might cause trouble to feed the antenna as straightforward as antipodal Vivaldi antenna.

To solve this problem, it is proposed to take a cubic volume from one of the substrates in such a way that the inner layer becomes touchable. Then, solder the middle pin of the SMA connector to the inner layer and the outer pins to the outer layers of the antenna. This approach and its consequences are studied in the next chapters.

To confirm the capability of balanced antipodal Vivaldi antenna and to start the process of optimization on this structure, although it has already shown promising characteristics, it is necessary to check its footprint. If the result of this experiment approves the capability of this antenna, it is, then, reasonable to start the optimization procedure.

To do this experiment, 966 probes are used to cover the area of 50×20 cm^2 which half of them are in co-polar and the other half are in cross-polar configurations. Thanks to the symmetry of balanced antipodal Vivaldi

antenna, this area is enough to capture the footprint of the antenna in the area of $50 \times 40\text{cm}^2$. For co-polar and cross-polar configurations, separately, peak-to-peak values of the main pulses, which are captured by the probes of that configuration, are depicted in figure 2.12. The image of co-polar configured probes confirms that the antenna has the capability to illuminate sufficient area on ground. On the other hand, the balanced antipodal Vivaldi emits cross-polarized field as it is appeared on the cross-polar probes (figure 2.12(b)), but it is not so tangible to cause trouble for detection process of GPR with this antenna. This can be seen in the co-polar to cross-polar ratio which is depicted in figure 2.12(c). This ratio is reasonably high for the detection area which antennas should illuminate on ground.

Knowing these prospects, it is possible to conclude that the balanced antipodal Vivaldi antenna can be improved to fulfill the requirements of this project and the optimization process can be started on this structure. The problem of feeding can be solved by the proposed method. Also, reducing the cross-polar fields is a concern in the project to be improved so that higher co- to cross- polar ratios are obtained.

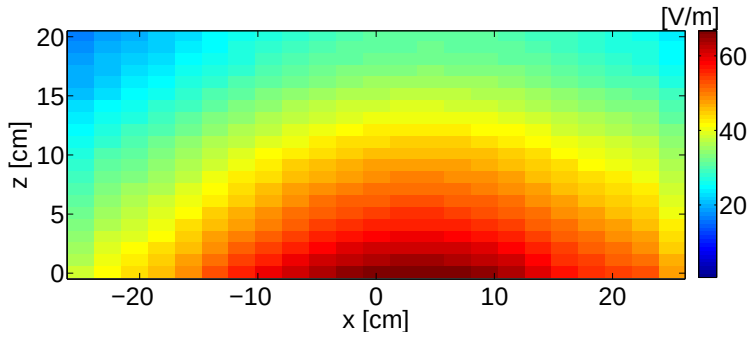

(a) Peak-to-peak Values of the Main Pulse of Co-polar Fields in Linear Scale

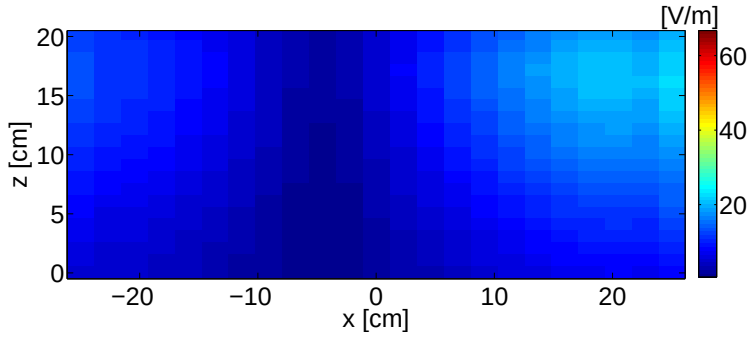

(b) Highest Peak-to-peak Values of the Radiated Pulse of Cross-polar Fields in Linear Scale

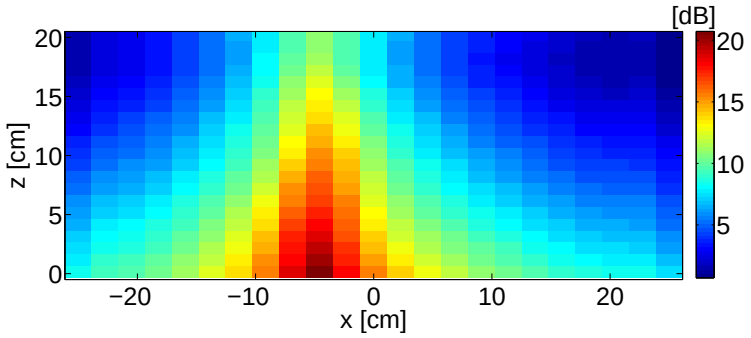

(c) Ratio of Peak-to-peak Values of Co- and Cross-polar in dB Scale

Figure 2.12: Foot-print of the Antenna Captured by Co- and Cross-polar Probes

Optimization of Balanced Antipodal Vivaldi Antenna

3

This chapter covers the main parts of the optimization process on the balanced antipodal Vivaldi antenna (BAVA) structure. The optimization process, as explained throughout this chapter, is from top to bottom in the sense that first the flares of the antenna are optimized in section 3.1. In section 3.2, the discovered common problem of many designed BAVAs are explained and as the main novelty of this work a successful solution is suggested. To complete the design of the antenna, the matching circuit design, optimization and simulation are studied in section 3.3. Finally, the entire structure of the antenna is simulated and the result of the simulation is reported in section 3.4.

The main goal of optimization in this stage is to achieve the required return loss characteristic over the operating bandwidth of the antenna.

3.1 Radiating Flares Optimization

The maximum width, W, of the antenna flares is the most important dimension in radiation of low frequency components. With an inadequate width, the low frequency components cannot be radiated even though the other parameters are optimized. On the other hand, choosing a large width makes the antenna costly. The importance of this parameter, both theoretically and practically in antenna design, is the cause to start the optimization procedure of the antenna flares with this parameter. A coarse search on

a reasonable range of widths is simulated as the first step. The searching range becomes finer based on the results of the coarse search so that a proper width can be found.

Knowing the width of the antenna, a fast-converging technique is used to optimize the lengths of the inner and outer curves in the antenna - L_i and L_o in figure 3.1, respectively. This part of the optimization is explained in section 3.1.1. Hence, by completing this step the dimensions of the flares are determined.

The next in the line is to optimize the curvatures of the flares. Theoretically, infinite number of exponential curves can be drawn for each triple of W, L_i and L_o. It is obvious that checking the result of these infinite number of curves needs infinite time. Thus, some assumptions from the antenna theory should be used in order to find the relevant parameter and try to optimize the antenna in an efficient way. More assumptions can also be made based on the current literature on design of BAVA. This is explained in-detail in section 3.1.2.

In all of the aforementioned steps, the goal of optimization is to find a set of parameters in such a way that the return loss of the antenna stays below -10 dB in the required frequency band, $0.3 - 6$ GHz. This will guarantee that the antenna is working in this frequency band, however, it does not guarantee the best (optimum) radiation characteristics. In other words, the return loss graph shows that the antenna has radiated the excitation pulse to what extent, but it is not possible to extract how, where and when the pulse is radiated. Optimization with respect to the radiation characteristics is discussed in chapter 4.

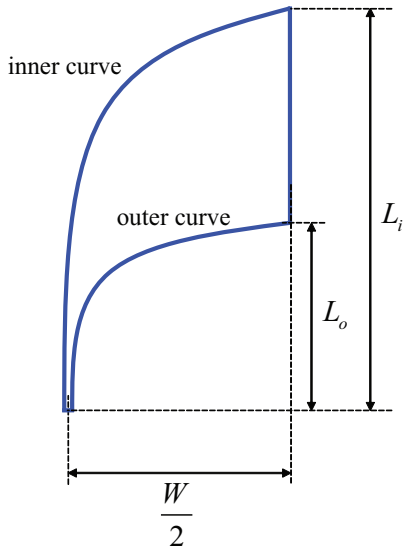

Figure 3.1: Primitive Schematic of Radiating Flares Geometry

3.1.1 Geometrical Dimension Optimization

Given that the width of the flares is larger than the length in BAVA, it is possible to use the theoretical limitation on the width of the antenna. An improved version of Chu-Harrington limitation is developed theoretically as follows [34],

$$Q_{min} \approx \frac{1}{ka} + \frac{1}{2\,(ka)^2} \tag{3.1}$$

where Q is the quality factor of the antenna and it is defined as the ratio of the time averaged stored energy around the antenna to the radiated power. a is the minimum radius of the sphere in which the antenna fits and k is the wavenumber on the antenna aperture. In the same publication, it is claimed that $\max \frac{G}{Q}\,|_{dir} = 60$. This is relevant for the Vivaldi antenna due to the fact that it is a directional antenna. The maximum gain of the Vivaldi antenna is

$$G_{max} = 8 \text{ dB} \equiv 10^{8/20}.$$

Hence,

$$\begin{aligned} Q_{min} &= \frac{10^{8/20}}{60} = 0.0419 \\ \Rightarrow ka &= 24.36 \\ \Rightarrow a &= 24.36\frac{\lambda_c}{2\pi} \approx 251.62 \text{ mm} \end{aligned} \tag{3.2}$$

Hence, the following values are chosen for the coarse search of the width of the antenna to start with:

$$W \in \{200, 300, 400\} \text{ mm}$$

Also, to have better understanding of radiation in various widths and to have better overview for each width, a number of inner and outer curves by various lengths are considered. The lengths which are considered in this experiment are as follows.

$$L_i \in \{200, 250, 300, 350, 400, 450\} \text{ mm}$$

$$L_o \in \{150, 200, 250, 300\} \text{ mm}$$

For each width, 13 models are made[1]. The return loss of these 13 models are averaged and depicted in figure 3.2. In high frequencies, as illustrated in this figure, the matching is better than -10 dB no matter which maximum width is used. That is obvious, though, because the higher frequency components of the pulse are radiated in much smaller width than 200 mm. Thus, they should be compared in low frequencies and this is the reason why the return loss graphs are plotted to 3 GHz, and not to 6 GHz. In figure 3.2, for $W = 300$ mm and $W = 400$ mm the same behavior can be seen in low frequencies, while $W = 200$ mm has worse return loss in low frequencies.

[1]The flare is considered when the inner curve is longer than the outer curve by at least 100 mm.

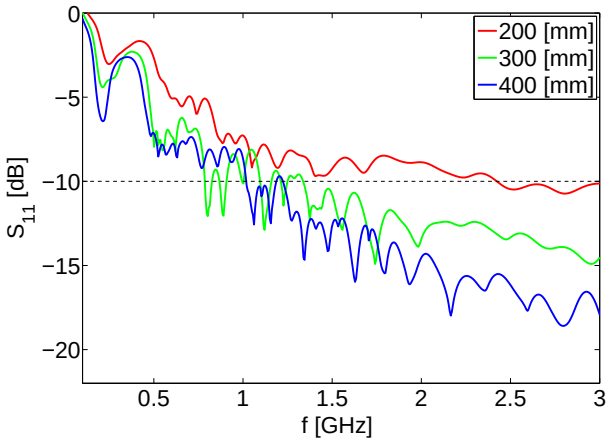

Figure 3.2: Averaged Return Loss of Models with the Same Width - Coarse Search

From this figure and by checking the return loss of all 3 models, it becomes clear that with widths near 200 mm radiation in low frequency is most likely impossible. While the width gets closer to 300 mm, the antenna radiates better in these frequencies. This behavior remains the same for larger widths and is improved. To have better view, the same experiment is done with finer steps of widths

$$W \in \{250, 300, 350\} \text{ mm}$$

with the same combination of curves and lengths as the previous coarse search. The result of this experiment is depicted in figure 3.3. This figure confirms that the behavior in low frequencies of the desired range is the same, while slightly better results can be expected in higher frequencies with larger widths. This means that the capability of radiation at such low frequencies as 300 MHz burgeons around $W = 300$ mm and will be enlarged when width reaches to $W = 350$ mm.

It should be noted that these experiments are simulated with CST MW Studio. The models are printed on a $\epsilon_r = 2.3$ substrate and are excited by a waveguide port.

Closeness of return loss graphs of $W = 300$ mm and $W = 400$ mm in figure 3.2 and the obtained results in the finer experiment shows that it is wise for the rest of the work to fix the width of the models to 300 mm and 350 mm. This diffident in choosing the width is due to the closeness of the results in these two widths and the important role of curvature of the flares in radiation.

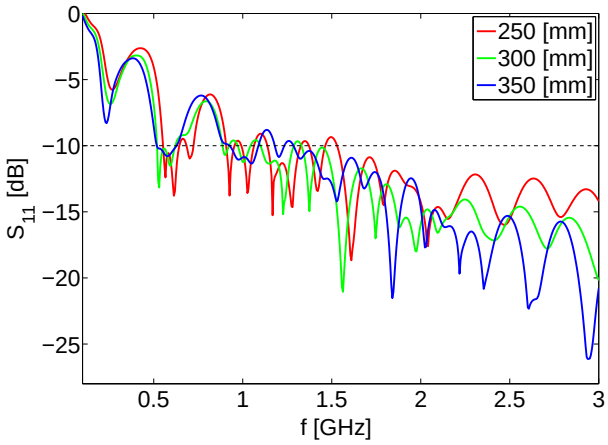

Figure 3.3: Averaged Return Loss of Models with the Same Width - Fine Search

Fixing the width to 300 and 350 mm, it is the time to optimize lengths of the curves. Nonetheless, the complexity in this step is increased because the radiation characteristics of BAVA depends not only on the lengths of the curves, but on curvature of the flares as well. For each triple of width, inner and outer flare lengths, it is still possible to draw infinite number of exponential curves. In this sense, with a same set of width and lengths, there might be some exponential curves which does not radiate at all while the curve with optimum results is also laid there! This is because the equations for determining the curves are taken in their most complete form and can have 6 unknowns (or constants) which separate each curve from the other one. The curves supports the assumption of having the width at the starting

point of the curves. These equations are followed:

$$\begin{aligned} x_{inner} &= -0.5\,(c_s + c_w) + c_s \exp\left(k_s {y_{inner}}^{n_i}\right), \\ x_{outer} &= -0.5\,(c_s + c_w) + c_w \exp\left(k_w {y_{outer}}^{n_o}\right). \end{aligned} \tag{3.3}$$

To find the optimized curves, it takes lots of time and does not seem so efficient to vary parameters blindly or coarsely. Instead of such boring method, a fast-converging method based on the Physics of Microwave has been suggested in which the curve is defined by *a pair of parameters* so that the lengths and curvature of the flare are tied together.

One parameter of this pair is ζ which indicates the slope of the orthogonal line to the curve at the certain point of the curves which is crystallized in figure 3.4. As depicted in this figure, ζ determines the slope of the curves at $(-x_1, y_1)$ and (x_1, y_1) for inner and outer curves, respectively. With this parameter, it is possible to control the opening angle of the flares. With higher values of ζ, radiation occurs earlier due to the openness of the antenna flares while with lower values the wave should travel along a transmission line before radiation.

Introducing ζ, 2 out of 6 unknowns can be determined in equation 3.3. The position of two points $(-x_1, y_1)$ and (x_1, y_1), as depicted in figure 3.4, solve one unknown as well. The system of 4-equations-7-unknowns is written explicitly in equation 3.4. In this system of equations, they are all related to the starting points of the curves (figure 3.4). This means that by changing n_i, n_o and ζ a pair of curves are defined and the lengths will pop-up. The values of the parameters are mentioned in Table 3.1. These values are chosen so that the lengths of the curves as well as their curvature are reasonable.

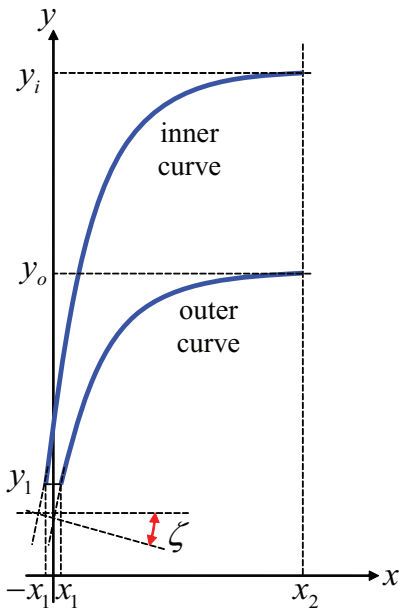

Figure 3.4: Slope of the Orthogonal Line to the Both Curves at $y = y_1$, ζ

Table 3.1: Values of the independent parameters in optimization of flares

Parameter	Value
ζ	0.0005, 0.001, 0.01
n_i	$1.4 - 5.0$
n_o	$2.8 - 4.3$

$$
\begin{aligned}
-x_1 &= -\frac{(c_s + c_w)}{2} + c_s \exp\left(k_s {y_1}^{n_i}\right) \\
x_1 &= -\frac{(c_s + c_w)}{2} + c_w \exp\left(k_w {y_1}^{n_o}\right) \\
\zeta &= c_s k_s n_i {y_1}^{(n_i - 1)} \exp\left(k_s {y_1}^{n_i}\right) \\
\zeta &= c_w k_w n_o {y_1}^{(n_o - 1)} \exp\left(k_w {y_1}^{n_o}\right)
\end{aligned} \tag{3.4}
$$

Over 100 models based on the parameters in the table 3.1 are created and simulated where only the flares of the antenna were included. They

are excited with a $0.1 - 6$ GHz impulse through the waveguide port in CST Microwave Studio. The return loss of each model is collected and fully studied. Finally, the optimum result is obtained which is depicted in figure 3.5. The parameters which were used to create this model and the shape of the flare are illustrated in this figure as well.

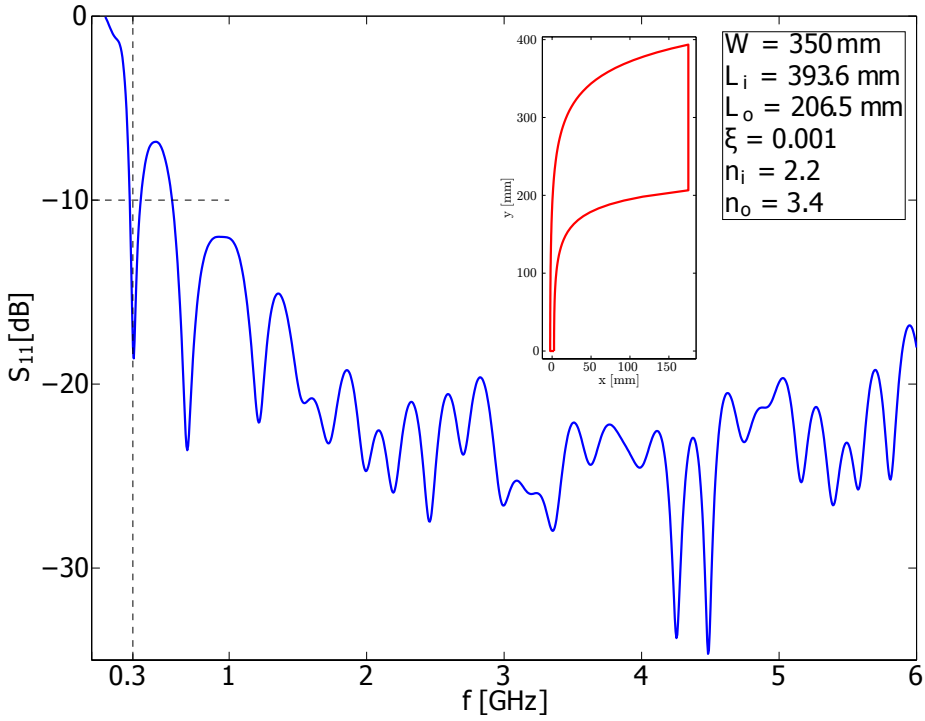

Figure 3.5: Optimum Return Loss, Including the Flare of the Antenna and Its Parameters

The S_{11} graph, which is depicted in figure 3.5, has an inconvenient peak just after $f = 0.3$ GHz. After this peak, which is higher than -10 dB, rest of the return loss graph laid below this threshold and shows a promising matching between the waveguide port and the flares. It should be emphasized that over 100 models are simulated and the optimum result is still not sufficient. Thus, to optimize the antenna for the entire required frequency band of 300 Mhz to 6 GHz more parameters or procedures should be involved.

3.1.2 Flare's Curvature Optimization

Actually, the reason why curvature of the curves should be optimized after the previous long processes of simulations is that the optimum return loss of the section 3.1.1 is still not satisfactory for the purpose of this project. Fortunately, there is a chance to optimize the curvature of the flares and it might help attaining better return loss graphs. In figure 3.6, a new parameter which shows the length of triplet line is introduced - L_v. This parameter is not used in previous simulations, but in the following curvature optimization it is used.

To start the optimization process, first, it is needed to rewrite the equations in another form such that the parameters of the curvature appear. These parameters are recalled in figure 3.6. The equations 3.3 are defining the curves which started from $y = L_v$. In this way, all the parameters in figure 3.6 are set such that the flare in this figure mostly fits the optimized flare of the section 3.1.1. Now by changing n_i or n_o the curvature will change while the other features remains the same. So, various exponential curves with different curvatures are modeled and simulated in this step of optimization. Nonetheless, there was no improvement in return loss graphs.

It is obvious that with different curves behavior of the antenna should change, but such difference will not be appeared in the return loss graphs. This issue, actually, has two sides. The positive side is that the return loss is not sensitive to changing the curvature of the flares while the lengths and width i.e., geometrical dimensions, are fixed. Therefore, different curves can be used to optimize other radiation characteristics of the antenna [2]. The negative side is that none of the curves in these simulations could either

[2]This is the main idea of chapter 4 where the focus is on radiation characteristics of the antenna.

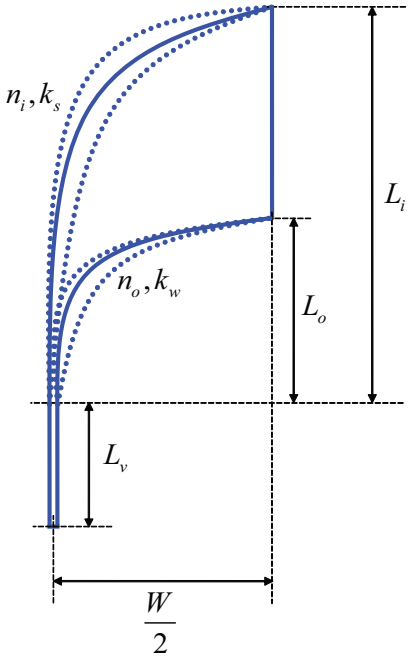

Figure 3.6: Parameters for Optimization the Curvature With the Same Lengths

improve or solve the inconvenient peak in the return loss. Therefore, there should be another source in this antenna which is hidden up to this moment.

3.2 Transition Disaster

Based on width of the antenna models and due to the extensive optimization process in previous sections, the optimized BAVA was prospected to operate over the entire required bandwidth. However, the return loss of the optimized antenna exhibits that, in spite of expectation for operating frequency band of $0.3 - 6$ GHz, it does not perform well in low frequencies. This is also approved by taking some samples of radiated pulses from the antenna. In this section, the physical reason(s) of this behavior is investigated in-detail and at last the solution is proposed.

3.2.1 Why is it called disaster?

To investigate this mismatch, it is logical to have a look at the returned pulse to the excitation port in time-domain. This returned pulse to the port *one*, $o_{11}(t)$, from which the antenna is also excited, is depicted in figure 3.7. In this figure, 5 pulses are distinguishable which are denoted with capital letters from A to E. The earliest one, A, is due to the first reflection from the excitation waveguide. This pulse can be used as an indicator of the time-line of the excitation i.e., the exact time when the pulse has entered the antenna and has been reflected. This time is not zero in CST because the excitation pulse starts with delay after zero, by default. The highest peak-to-peak value belongs to the pulse which is reflected from the end of the antenna, E. So, the time-line based on the earliest and latest pulses can be discovered.

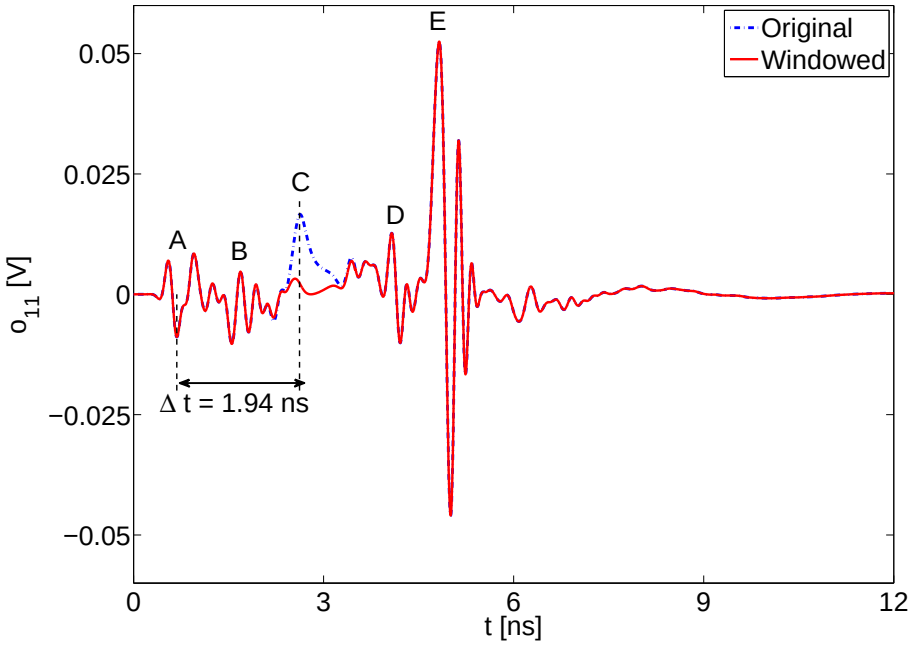

Figure 3.7: Returned Pulse to the Excitation Port - o_{11}

The idea is to remove these pulses one-by-one and see if the inconvenient peak in the return loss of the optimized structure is due to one of them explicitly or to a summation of these returned pulses. In this way the source for this problem can be figured out and thus it can be either solved or at least improved so that the peak will be alleviated.

For filtering the pulses in time-domain, *hamming* window is chosen as the basis of the time filtering function with the width of one excitation. This windowing function is selected based on its smooth frequency domain characteristics so that it does not affect the return loss, itself. The window size, as mentioned earlier, is specified by the time duration of the excitation pulse so that when it is applied to the return pulse of o_{11}, it filters only one pulse out. In this way, the reflected pulses can be removed one-by-one to study their impact on the return loss in frequency-domain. This is possible by referring to the definition of the return loss

$$S_{11} = \frac{\mathcal{F}\{o_{11}\}}{\mathcal{F}\{i_1\}}$$

Thus, the *fft* of the excitation pulse which remained the same for all of them and the filtered data are calculated and used to update the return loss graph.

Interestingly, by removing the pulse which comes 1.94 ns later than the excitation pulse, C, the S_{11} requirement can be met (figure 3.8). Figure 3.8 determines that the removed pulse from time-domain returned pulse has the frequency components between 0.3 and 3 GHz. This is not the case for other pulses, though. In other words, if one of the remained pulses was removed i.e., B, D or E, the return loss in frequency domain would have been improved in high-frequency or in entire frequency band which in either case the annoying peak in frequency-domain remains.

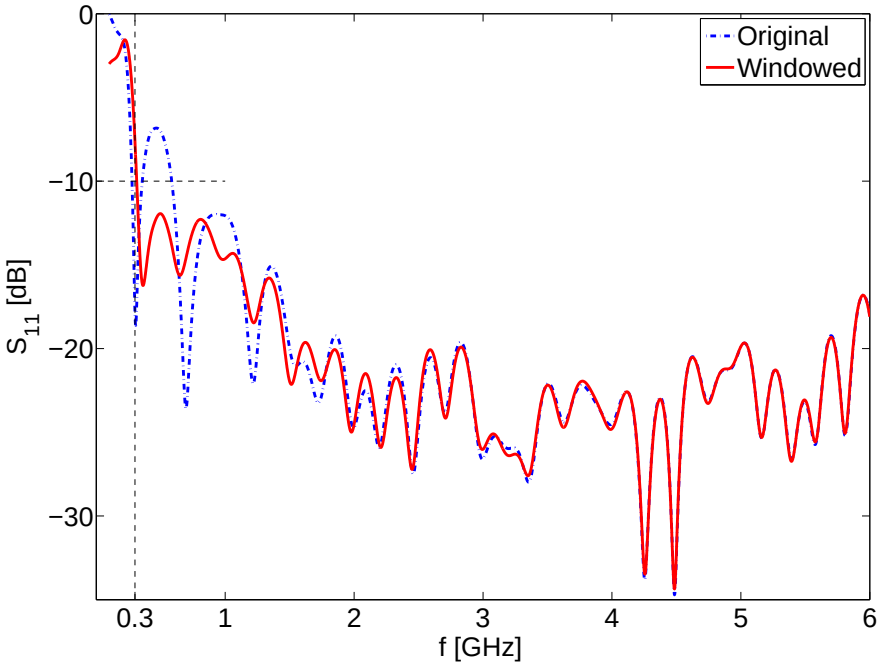

Figure 3.8: Returned Loss Before and After Windowing the Returned Pulse From the Bottleneck of the Antenna

The returned pulse C is, basically, reflected from the transition of triplet transmission line - the part which was indicated by L_v in figure 3.6 - to the port. This exactness of the location of the returned pulse can be confirmed by checking the wave velocity on the flares and using the time difference between the excitation pulse and the returned pulse.

$$\begin{aligned} \Delta t &= 1.94 \text{ ns} \Rightarrow \\ r &= \frac{\Delta t}{2} \cdot v_{wave} \\ &= \frac{1.94 \times 10^{-9}}{2} \times \frac{3 \times 10^8}{\sqrt{2.33}} = 0.1906 \text{ m} \approx 190 \text{ mm} \end{aligned} \tag{3.5}$$

Normally, the low frequency components of the pulse are supposed to be radiated in the outer parts of the flares i.e., near the ending of the antenna. However, the position of this returned pulse on the antenna shows that

the frequency components between $0.3 - 3$ GHz of the excitation pulse do not have any chance to be radiated even though the flares are wide and large enough to radiate them. They have already reflected from transition to the flares back to the waveguide before they reach the radiating flares. $r = 190$ mm addresses, actually, the location on the antenna where the flares start tapering to the sides.

Lack of these frequency components can be seen in the radiated pulses of the antenna. To observe this, the radiated pulse is captured via a probe located 1 m away from the waveguide port in simulation in the center. It is oriented in co-polar direction. The radiated pulse is shown in figure 3.9. This figure, clearly, shows that the radiation in low frequency components which is emphasized by two hatched-lines is much less than the radiation in higher components. The radiation in low frequencies might be influenced by the omni directional pattern of the antenna. However, that effect is less than a few dBs. To confirm this lack of radiating in low frequencies, the same scenario has been simulated with a dipole. The testing dipole antenna has the same length as the maximum width of the BAVA and the probe is located in the same position and with the same orientation. The result of this experiment shows that the radiation at 0.3 $\{GHz$ is the same, however, the BAVA radiates less at 0.35 or 0.4 GHz.

So, there is a *bottleneck* in the antenna which does not let low frequency components of the pulse pass through and being radiated on the flares where they were supposed to be radiated, no matter how much wide the antenna is designed. This disaster can be seen in many recent BAVAs which are designed so far [11], [35], [36] and [37].

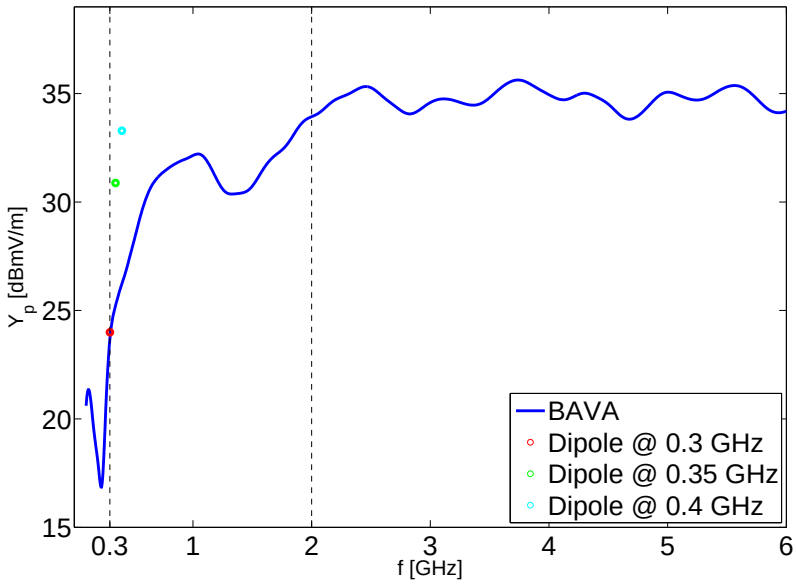

Figure 3.9: Radiated Pulse of BAVA, Captured 1 m away from the waveguide port in the center of E-plane

3.2.2 Solutions to Transition Disaster

Up to this point, it is made out by all simulations that the transition problem is due to the transition from triplet transmission line to the flares. Actually, none of the optimizations on the curves, flares, and geometrical dimensions could remove the annoying peak from return loss. To resolve the transition disaster, the Physical reasons behind this behavior must be considered and removed.

Actually, this reflection occurs due to rapid change in the impedance of the transmission line (figure 3.10). In the transition, the antenna starts radiating high frequency components while for low frequency components it is still a transmission line. Due to this different electromagnetic characteristics of the triplet and the transition sections, the transition cannot be handled by low frequency components and they will be reflected. To solve

this problem two solutions can be proposed.

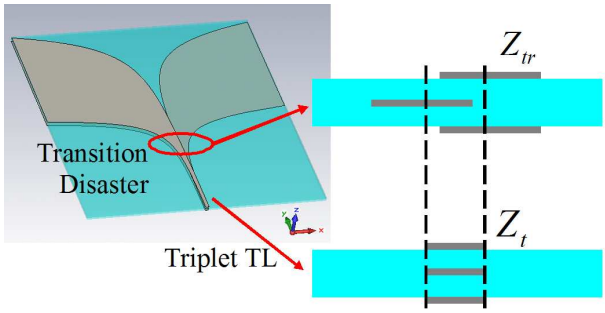

Figure 3.10: Cross-section of the Antenna at Triplet Transmission Line and Transition to the Flares

- First Solution: To make the transition smoother, both curves should be tapered up. This idea was simulated by various curves and it was not successful. Apparently, this method has not only been applied on many simulations in this work but also in other works on the BAVA.

- Second Solution: the overlap of triplet transmission line is diminished before the transition to the flare in the line has been started. This is realized by shifting each metal layer to the direction of the opening of the flare of that layer. If the flare is opened in $\hat{x}$ direction, the metal layer will be shifted to $\hat{x}$ direction, otherwise to $-\hat{x}$ direction. In this way, the overlap will be disappeared from triplet line of the figure 3.10.

The optimized flares of the section 3.1 with the second approach is simulated. Result of this approach exhibits achieving the goal successfully. The annoying peak from the return loss as well as the reflected pulse from transition in the antenna are removed. The return loss of the antenna is depicted in figure 3.11. This figure shows that the disaster is resolved in this Vivaldi antenna, also by checking the reflected pulse to the port, it is possible to

see that the most of reflection is from the end of antenna where significant improvements can be done, specifically on the sharp edges at the end.

The most important and the main novelty of this Thesis in designing an UWB antenna in comparison to other similar works in recent years has been achieved by this result. This is a solid proof which shows that the designed antenna is capable to radiate over the entire desired ultra-wide frequency band. The antenna, thus, should be connected to the end-launch and then the investigation on radiation characteristics can prove the capabilities of this BAVA. The explanation of this piece of optimization process is kept for chapter 4.

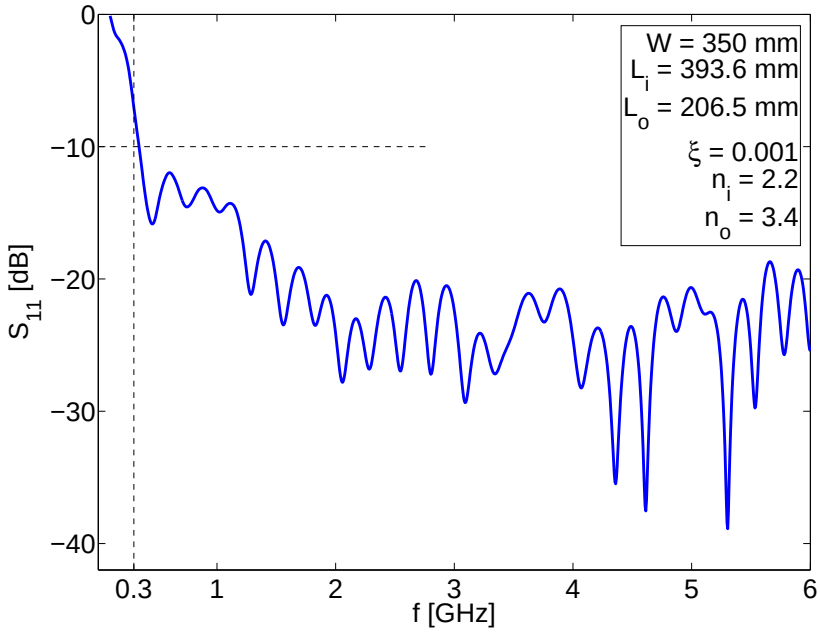

Figure 3.11: Return Loss of the Optimized Structure, Applying the Second Approach of Bottleneck Removal

3.3 Matching Circuit Design and Optimization

In section 3.2, the transition disaster is discussed and a solution has also been proposed in section 3.2.2 to solve this common BAVA problem. Based on the solution, the transmission line which matches the antenna impedance to 50 Ω feeding line takes a new and different structure as well. The idea in the solution is to avoid overlap between projected images of the flares on the plane parallel to the antenna flares as introduced in previous section. As a consequence, the matching transmission line needs to be designed based on the new flares' structures. The matching transmission line carries, basically, the pulse from the 50 Ω feeding coaxial cable to the antenna flares where the impedance is higher and is imposed by the radiating characteristics of the antenna.

3.3.1 Cross-section of Transmission Line at Different Locations

To start designing the first part of the matching transmission line, a stripline seems promising. Adjusting the width of the line, it can provide the antenna with 50 Ω impedance over a wide range of thicknesses and dielectric permittivities. This flexibility helps to reduce the cost of the antenna by choosing over wide range of commercial materials in the market. Also, the stripline is a stable structure in frequency and it is easy and suitable to be soldered to the end-launch pin.

Thus, the transmission line is started with a stripline. The cross-section of this stripline is depicted schematically in figure 3.12(a). In this figure, the dielectric is transparent to have a better view of the line. The stripline should be tapered somehow to the same cross-section of the starting point of the antenna flares which is illustrated in figure 3.12(b).

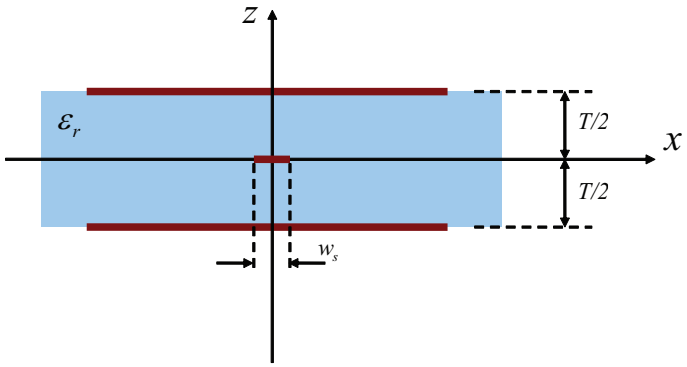

(a) Starting Cross-Section

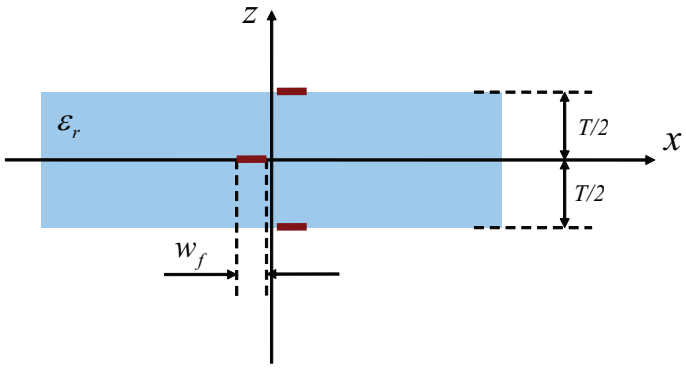

(b) Ending Cross-Section

Figure 3.12: Cross-section of the Stripline at Starting and Ending Points of the Matching Transmission Line

Figure 3.12(a) shows the cross-section of the matching part of the entire antenna at the beginning where it should be connected to the 50 Ω end-launch i.e., the point where the coaxial cable is going to be connected. The transmission line should be designed in such a way that connects these two cross-sections and, concurrently, overcome two sources of reflection: the geometrical discontinuity in the structure and the line impedance discontinuity.

The latter, impedance discontinuity, can be solved by smoothly varying

the width of the transmission line [38]. The width can be used to find the best impedance matching between the flares and transmission line. The impedance of the line is a function of thickness and permittivity of the substrate as well. But, once these parameters are fixed to match the line to the 50 Ω at the beginning, they cannot be changed for the rest of the transmission line.

Now, the challenge is how to transform the transmission line from the starting cross-section to the ending cross-section so smooth that the reflection would be less than −16 dB. Evolving with the impedance matching, this challenge has two parts: first, how to keep the line smoothly tapered with respect to the geometry and, secondly, how to keep increasing the impedance of the line from starting point to the impedance of the flares which is imposed by its radiation characteristics.

There are different structures which can transform the initial stripline to the antenna flares. Among these models, two of them seem to be the most consistent structures for this purpose in the sense that geometrical discontinuity in them are kept as low as possible while the length of the structure is tried to be shortened. Also, they have enough number of parameters to optimize and achieve the required feature.

In figure 3.13, the proposed transmission line structures are delineated. This figure is the top-view of a three-layer line which is started with a stripline and ended to the overlap-less triple transmission line (figure 3.12(b)) which is a novel transmission line. The line with red color shows the border of the middle metal layer while the blue color shows the metal layers on top and the bottom of the structure. Two layers of substrate are skipped in this figure, but they will be positioned between these three layers of course.

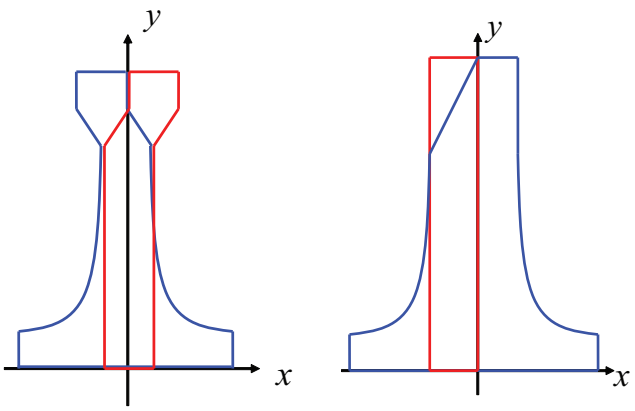

(a) Symmetrical Double Mitered

(b) Unsymmetrical Single Mitered

Figure 3.13: The Proposed Structures to Transform the Stripline to the Antenna Flare's Entrance

In figure 3.13(a), red and blue transmission lines both are mitered and in figure 3.13(b) one of them is mitered. This is why they are called "double" and "single" mitered, respectively. The reason why mitered structures are proposed is that these structures provide the designer with more number of parameters to change and optimize. For instance, angle, size and position of the mitered line can be used for optimization, while bent structures are identified by a radius.

The proposed structures are simulated based on the parameters of the line. The simulations show that the symmetrical single mitered structure performs better than the other one. The reason for higher performance is the middle layer. The middle layer in the double mitered line is mitered which introduces geometrical discontinuity while it is kept straight in symmetrical single mitered structure. Therefore, this design will be used to proceed with this structure.

After all of these simulations, the symmetrical single mitered structure

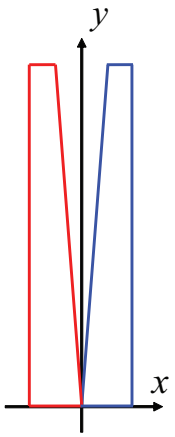

Figure 3.14: The Final Tapering of Transmission Line, the Scissor-like Transmission Line

still has a different cross-section from the starting point of the antenna flares. Obviously, it should be changed to the starting of the flares. A simple scissor-like structure is used to connect the single mitered transmission line to the antenna starting point. Figure 3.14 shows how this transformation is accomplished. The color code in this figure is the same as figure 3.13. In this transmission line, basically, by varying the width of the line similarly for all three layers, it is possible to control the impedance of the line. This is important because at the end the input impedance of flares are much less dependent on the width of the lines than its radiation characteristics. In other words, the input impedance of the flares are imposed by radiation characteristics of the antenna and not by the width of the starting point. So, the width of the scissor-like transmission line should be optimized to match the input impedance of the antenna. This optimization process has been fully investigated later in this chapter.

The two structures in figures 3.13(b) and 3.14 are attached together at last to realize the entire matching transmission line (MTL). The complete MTL can be seen in figure 3.15. This figure shows different parts of the line

as well as the parameters which used to define this line.

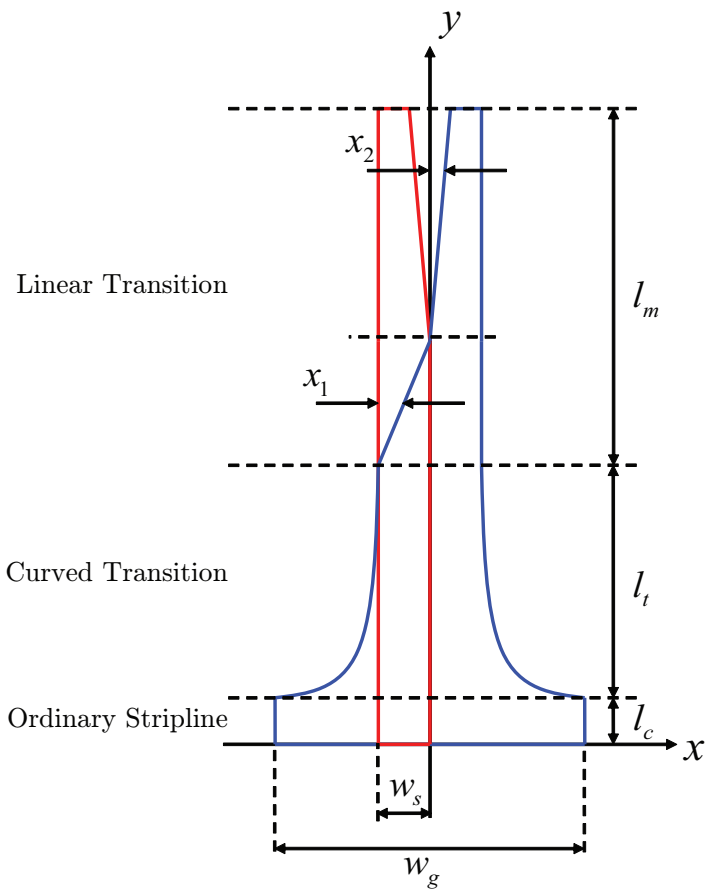

Figure 3.15: The Entire Matching Transmission Line and Its Parameters

3.3.2 Optimization of MTL

Figure 3.15 delineates the entire MTL. This structure consists of 3 parts which are designed and optimized in the following sections. The first part is an ordinary stripline - a stable structure to match the 50 Ω input impedance of the feeding coaxial cable. The second part in this structure is the curved transition from the stripline to the single mitered stripline. Finally, the third part is the single mitered stripline and scissor-like stripline which are

attached to each other.

For each part, the optimization has been done distinctly. Then, they are simulated altogether and refined.

3.3.2.1 The First Part: Stripline

The first part in this series which has to be designed is the ordinary stripline. The importance of designing the stripline is the fact that this line can be used to identify the material of the substrate and, consequentially, parameters of the substrate. In fact, the width of middle metal layer as well as thickness and permittivity of the substrate are sufficient to calculate the impedance of this line, theoretically. These parameters are illustrated in figure 3.16. T stands for the thickness of the substrate in this figure as well as the following equations. There is a difference between the thickness of the substrate in theory and practically designing an antenna. In theory, the thickness of the substrate is the distance between two ground layers of the substrate. In practical designs, however, due to the fact that each metal layer should be printed on a substrate sheet, the thickness refers to the distance of the ground layer to the middle layer. Actually, that is the thickness of the substrate the designer will order. This small but noticeable issue has been considered and that is the reason why in figure 3.16, T has been shown as twice $T/2$. So, in calculation, T has been used as the thickness of the substrate, while $T/2$ is used in simulations, finding the material, etc. w_s and w_g are the width of the line and the width of ground layers, respectively. The ground layer width is not specifically determined but in the following its importance will be clarified.

The commercial materials in the market are available over a limited quantized standard thicknesses and also limited range of permittivities. Thus,

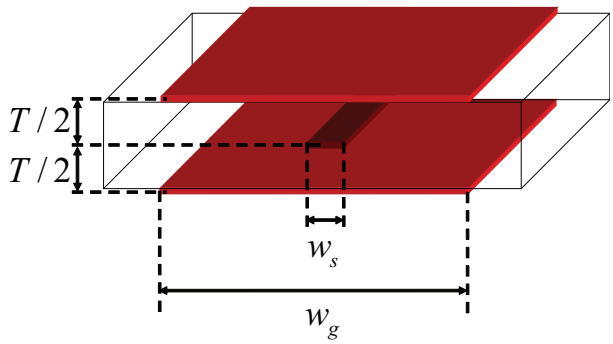

Figure 3.16: The 3D View of the Stripline Structure

the only parameter remains to play with is the width of the stripline. Theoretical background in the design of stripline can be found in many transmission line references. Based on full-wave approach, these equations are derived as follows [39]:

$$Z_0 = \frac{30\pi}{\sqrt{\epsilon_r}} \frac{1}{0.441 + w_{se}/T} \tag{3.6}$$

$$\frac{w_{se}}{T} = \frac{w_s}{T} - \begin{cases} 0 & w_s/T > 0.35 \\ (0.35 - w_s/T)^2 & w_s/T < 0.35 \end{cases} \tag{3.7}$$

where Z_0 is the impedance of the line, ϵ_r is the permittivity of the substrate. w_{se} is the effective width of the strip which is derived in the formulas. By Manipulating equations to have w_s/T as a function of ϵ_r:

$$\frac{w_s}{T} = \frac{30\pi}{Z_0\sqrt{\epsilon_r}} - 0.441. \tag{3.8}$$

By replacing the 50 Ω instead of Z_0 in equation 3.8, the following is derived:

$$\frac{w_s}{T} = \frac{3\pi}{5\sqrt{\epsilon_r}} - 0.441. \tag{3.9}$$

In equation 3.9, substrate permittivity can be found as a function of

w_s/T. This relationship is depicted in figure 3.17. The curve of this figure helps finding a suitable material for this project.

One of the commercial materials that are used for different purposes in PCB designs, is *RT/duroid 5870*. It has a relative permittivity of 2.33. Due to the fact that there are many materials in market in this range of permittivity, choosing this material makes the design more flexible in the sense that if at the end the need for a little higher or lower permittivities are seen, it is then possible to choose another material very close to this one as the substrate. *Rogers RT/duroid 5870* can be ordered with the thickness of 3.175 mm. With this permittivity and thickness and by following the curve of figure 3.17, the width of the line is calculated as follows:

$$\begin{aligned} 0.794 &= \frac{w_s}{T} \Rightarrow \\ w_s &= 0.794 \times T = 0.794 \times 2 \times 3.175 \\ &= 5.042 \text{ mm}. \end{aligned}$$

The simulations also confirm $w_s = 5$ mm.

The previous equations on stripline are valid if the ground plate is at least 5 times wider than stripline width, i.e.,

$$w_g \geq 5w_s. \tag{3.10}$$

This is the minimum of w_g i.e., the choice of w_g can be larger than this minimum if required in optimization process. In addition to the ground plate width, in order to have a full-balanced wave propagating to the balanced structure of the antenna this stripline should be at least $\lambda_{min}/30$. λ_{min} is the minimum wavelength in the operating frequency band, hence:

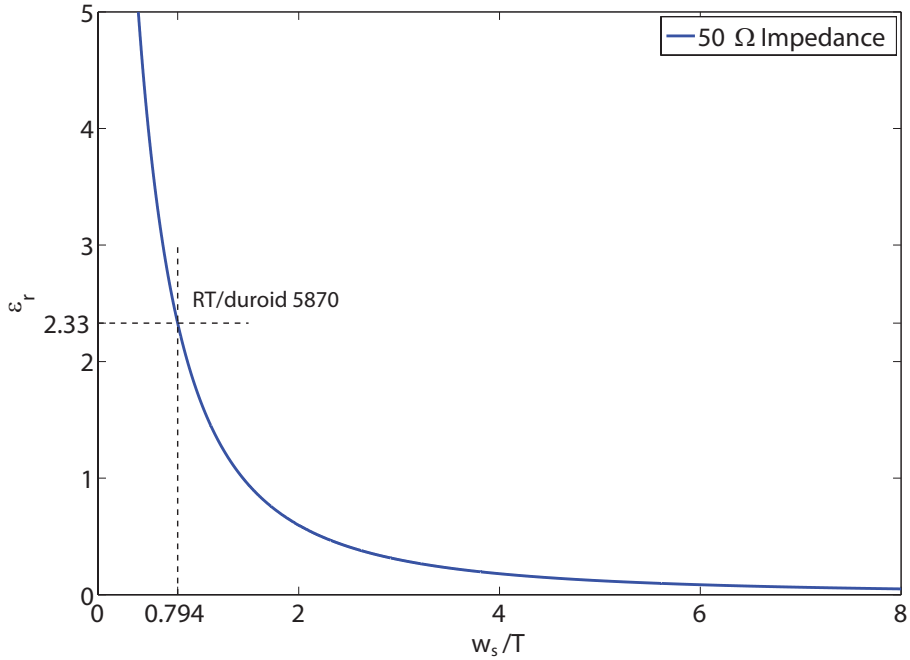

Figure 3.17: 50 Ω Impedance Stripline, Based on equation 3.9

$$\begin{aligned} \lambda_{min} &= \frac{c_0/\sqrt{\epsilon_r}}{f_{max}} \\ &\Rightarrow \lambda_{min} < \frac{c_0}{f_{max}} = \frac{3\times10^8}{6\times10^9} = 0.05\text{m} = 50\text{mm} \\ &\Rightarrow l_c \geq \frac{50}{30} = 1.66\text{mm} \end{aligned} \tag{3.11}$$

Based on equation 3.11, the required minimum for l_c is 1.66 mm. This is sufficient to claim that the stripline is a transmission line which obeys the curve of figure 3.17 and other expected characteristics. However, this length is not sufficient to solder the pin of the end-launch which is normally around 3 mm. Thus, $l_c = 5$ mm seems to meet both practical and theoretical requirements. Longer lengths might increase the total length of the antenna while it is not really necessary.

So, this part of the transmission line is designed based on theoretical ap-

proach. Optimization process of the line approves the theoretical consideration and leads to the very accurate matching to 50 Ω input impedance. The designed stripline with the aforementioned dimensions attains $Z_{in} = 49.96\ \Omega$ at $f = 3.05$ GHz.

3.3.2.2 The Second Part: Curved Transition

This is the part of the line where the transition from the designed stripline to single mitered line occurs. Over this transition, the characteristics of the stripline does not obey equation 3.8 anymore. Actully, formulation of stripline is not valid because the width of the ground is less than the minimum width of w_g (equation 3.10). So, for tunning the impedance the only possibility is to use the simulation tool due to the fact that characteristics of this line could not be found in the literature.

The design of this part is not separate from the previous parts. So, in all the simulations in this step the stripline is used as the basis. Also, in order to obtain the results the triplet line has been extended at the end of transition. This is the only possibility to observe the characteristics of the transition part using CST MS.

The goal is to design a curvature for this transition. The optimum curvature which smoothly connects the stripline to single mitered line should be designed such that the return loss becomes less than -16 dB over the desired frequency band. Also, the constant group delay is required.

Therefore, two approaches are used in order to obtain the best size and curvature. In both approaches, the stripline width w_s, thickness T and material are based on the selection in the section 3.3.2.1 and are directly inserted in the models of this section. w_g, the width of the ground layer, of the first part is the only parameter which will be optimized in this section

due to the dependency of the curvature on this parameter. As mentioned earlier, w_g has a minimum and no maximum. So, it can be chosen such that the minimum requirement has been seen.

1st Approach - Maximum Intercept : To find the optimum curvature in this approach, two rules are applied to all graphs with the form of

$$\mathbf{\Gamma_1}\,(x,y) \;= \{(x,y)\,|y = A_1 \exp\left(B_1 x^{n_1}\right) + C_1\}$$

which connect p_1 and p_2 (figure 3.18).

1. The difference between slope of orthogonal line to curve at p_2 and the horizontal axis should be smaller than a certain value i.e., ξ. With this, the continuity can be guaranteed and the electromagnetic wave will not be reflected from that spot due to a rapid change or sharp edge in the line characteristics.

2. The intercept of the orthogonal line to curve at p_1 with y-axis should be maximized. This rule is based on the anticipation that the reflection from the transition curvature at the beginning can be minimized. In other words, it is expected that less energy being reflected from transition to the feeding.

It is obvious that by increasing w_g the maximum y_b will get smaller. Thus, w_g should be set to its minimum. This minimum, as mentioned previously, comes from equation 3.10. Based on these two rules, the optimum size for l_t should be found by simulations. 6 models are created and simulated in which l_t is in the range of $10 - 60$ mm. For each model, the curve is calculated based on aforementioned rules.

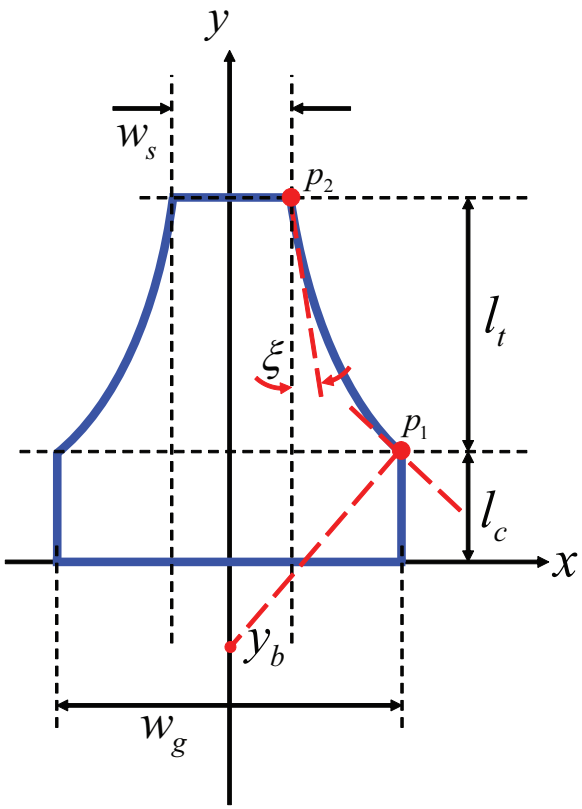

Figure 3.18: The Maximum Intercept Approach for Optimizing the Transition Curvature

The best result among these models, however, did not meet the requirements of the transmission line described previously. The group delay and reflection of the antenna are not constant and has many peaks, respectively. Briefly, this approach did not follow the physical assumptions behind its rules. So, there is no point to continue with it.

2nd Approach - Radius of Osculating Circle : In this approach, again two rules are applied to find the optimum dimensions and curvature of

$$\mathbf{\Gamma_2}\,(x,y) \;= \{(x,y)\,|y = A_2 \exp\left(B_2 x^{n_2}\right) + C_2\}$$

which connects p_1 and p_2. The rules are

1. The same as the first rule in First Approach. The difference between

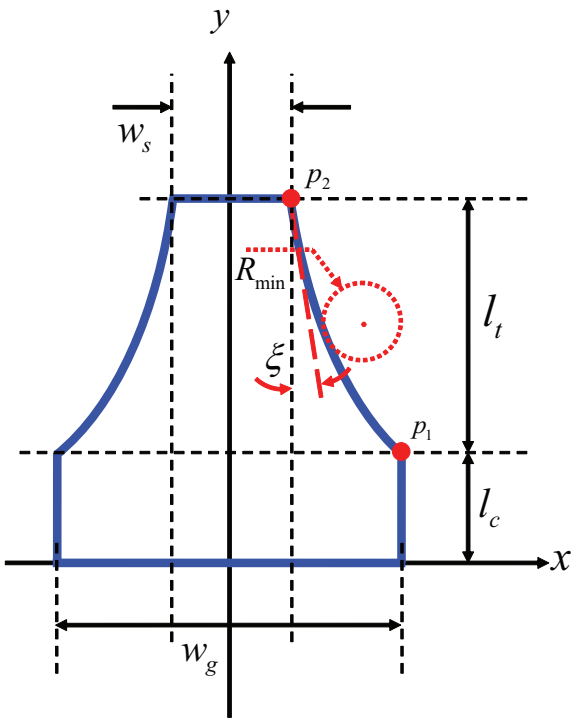

Figure 3.19: The Osculating Circle in the Second Approach

slope of orthogonal line to curve at p_2 and the vertical axis should be smaller than a certain level i.e., ξ. Although the first approach was not successful, it seems that this rule has a Physical basis and the first approach was unsuccessful because of its second rule.

2. The minimum radius of osculating circle, $R_{min}(x)$, over the curve should be maximized (figure 3.19).

By definition, the minimum radius of osculating - kissing - circle on a curve shows the point in which the curve has its maximum curvature. It is obvious also from the mathematical description of the oscillating circle radius $R(s) = 1/\kappa(s)$, where $\kappa(.)$ is the curvature of a curve and can be

calculated as:

$$\kappa\left(x\right)=\frac{\left|y^{''}(x)\right|}{\left(1+y^{'2}(x)\right)^{3/2}} \tag{3.12}$$

By maximizing $R_{min}\left(x\right)$, the curve becomes the smoothest curve between p_1 and p_2 which can also meet the first rule. However, this curve is not the smoothest curve for a certain l_t, yet. In other words, for a certain l_t, playing with w_g it is possible to find the smoothest curve. This work has been done and for each l_t the smoothest curve by considering the w_g has been used in simulations. By increasing l_t to find the smoothest curve, optimized w_g clearly increases. This introduces longer transmission lines which leads to longer antennas which it is not competent. Thus, the shortest line is an optimum which compromises all aspects of the transmission line and antenna design. The shortest line, comes with the minimum w_g based on equation 3.10. Hence, based on this width the shortest length and smoothest curve have been designed. The simulation results verify the physical expectations, indeed, and for $l_t = 10$ mm the optimum result is obtained.

3.3.2.3 The Third Part: Linear Transition

Knowing the fact that the thickness of the substrate and its permittivity are fixed, the impedance in the third part will be a function of x_1 and x_2 for single mitered and scissor-like transmission line, respectively. These two parameters are illustrated in figure 3.15. The relationship between each of these parameters and the impedance of such inventory lines can be figured out using simulation tools such as CST MS. For this purpose, each line has been designed related to its parameter, x_1 or x_2. Then, by changing the parameter, the input impedance of the line is taken as the result. The

results of these simulations are depicted in figures 3.20(a) and 3.20(b).

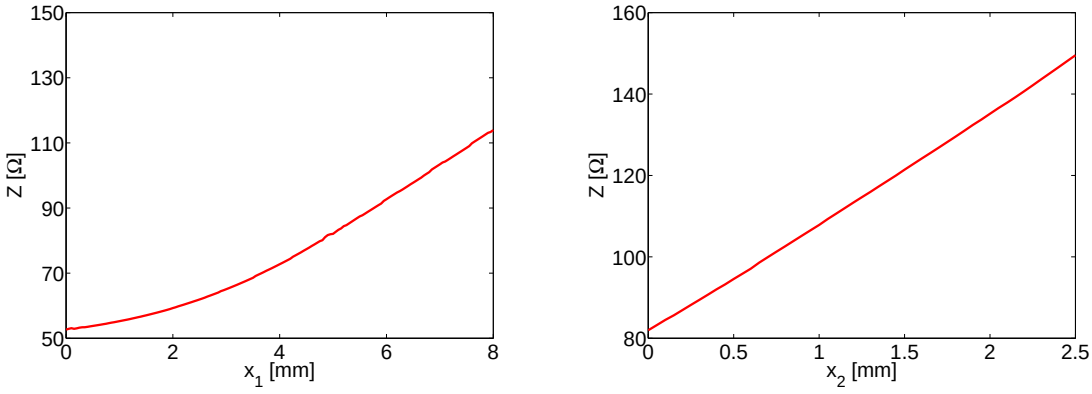

(a) Single Mitered TL Impedance as a function of x_1

(b) Scissor-like TL Impedance as a function of x_2

Figure 3.20: Impedance of the Transmission Lines in the Third Part as a Function of Their Width

Now, it is possible to make these transitions smoother. Instead of a line to connect the two ends of each part in the third part (figure 3.15), more points are used. Each point is chosen to create a predefined impedance increment. Knowing the total length of two parts, l_m, impedance at the end of second part and at the end of the third part, the number of points to be used for these two sections can be computed. This is a variable to make the antenna smoother as well. By choosing more points over longer lengths, the line might be smoother. The trade-off is on the length and the performance. So, this parameter provides the designer with the capability to choose the desired length and the impedance step size for the transmission line to reach the end impedance. The end impedance will be adjusted to match the input impedance of the antenna.

Eventually, the line will be created based on a linear impedance profile. After sufficient number of simulations, the shortest length is chosen so that

the requirement for the entire transmission line can be met.

This length can be verified and similarly found in different articles. It has been shown that for a transition from Z_0 to $3Z_0$ in wide frequency band of $4.5:1$, the length of the line should be more than $0.5\lambda_{max}$ to achieve $-20dB$ return loss [38], [40], [41]. Of course this length cannot be independent of the ending impedance of the line. In the next section a discussion has been done in this respect and the achieved results are compared with those aforementioned references.

3.3.3 Optimization of the Ending Impedance

There is still one parameter to optimize as mentioned earlier in this chapter. The ending impedance of the transmission line can be optimized such that the transmission line matches the antenna input impedance. The impedance varies if the width varies when permittivity and thickness of the substrate layer is kept fixed. The width as delineated in figure 3.15 is parameterized by x_2. By increasing x_2, the impedance of the line will be increased as demonstrated in figure 3.20(b). The range of 80Ω to 120Ω is chosen as an appropriate range for this optimization. For each impedance the width will be set based on the figure 3.20(b). Also, the starting width of the flares is set to the same width of the ending transmission line. This is necessary to avoid geometrical discontinuity and that will not change the input impedance of the antenna as that impedance is imposed by radiation characteristics of the antenna. Reflection to the port i.e., return loss, shows the mismatch in the line. Thus, return loss is taken as the result of each simulation and compared.

Figure 3.21 shows the result of the optimization of the ending impedance

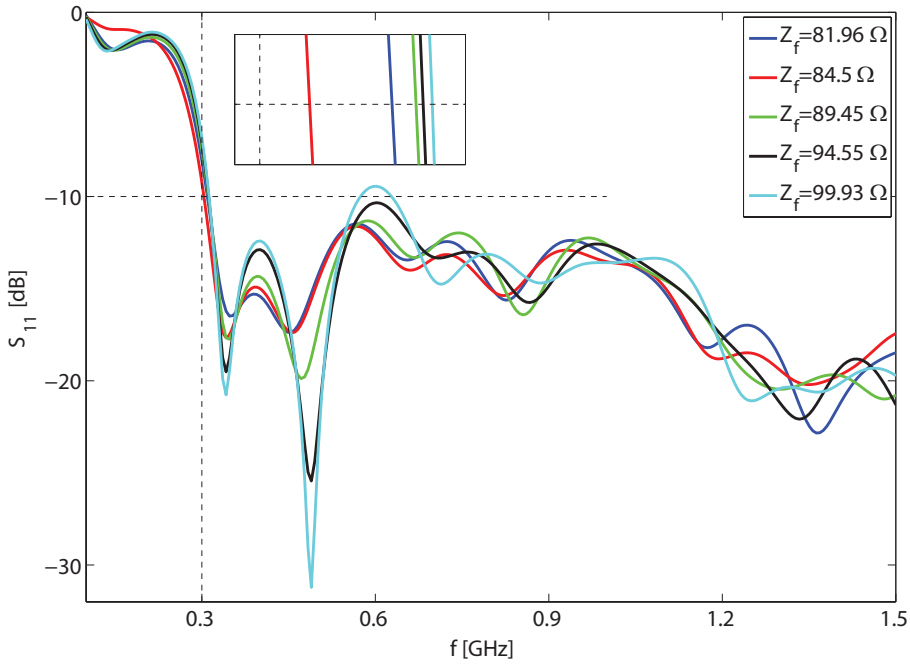

Figure 3.21: Return Loss w.r.t. to Various Ending Impedance of the Transmission Line

of the transmission line. In this series of simulation, the length of the transmission line is the same for all the models. The length of the inner and outer curves of the flares for each simulation varies, though. This variation is so small that can be neglected. The final impedances, Z_f, are illustrated as the legend in the figure. Although the results are up to $Z_f = 120\ \Omega$, the figure covers the simulations up to $Z_f = 100\ \Omega$. These results actually encompasses the rest which is skipped. The block inside the figure is the area around the -10 dB and 0.3 GHz which is zoomed in to have a better view.

From this result it can be seen that the final impedance is very close to $Z_f = 84.5\ \Omega$ than the others. The red line in this figure crossed the -10 dB before the others and also it has lower peaks afterwards. The result of the simulation in this sense clearly shows a local minimum around this final

impedance. This reason confirms why the choice of the same length for all simulations does not affect the result. If that was the case $Z_f = 81.96\ \Omega$ would have been the best result.

With this result, the design of the transmission line has been completed and all the parameters are optimized. In the next section, the transmission line is attached to the flares and, for the first time in this Thesis, the BAVA will be completely simulated.

3.4 BAVA Models with the Designed MTL

In this section, the optimized model of the previous sections are incorporated into one model. This is, thus, the optimized BAVA flares with the MTL included. The antenna is tested to see the overall performance with respect to the return loss.

To continue with the models and to find the optimum antenna design, four models are selected and simulated to observe the radiation characteristics. The return loss of these antennas will meet the required bandwidth thanks to the smooth design of the MTL and bottleneck removal. So, radiation of the antennas can also be studied to find the optimum model.

To create these four models two ending impedances, $Z_f = 81.96\ \Omega$ and $Z_f = 84.5\ \Omega$, from the previous section are chosen. These two impedances show higher performance over the others with respect to return loss. Although return loss is not sufficient, it is one the most important features without which the UWB characteristics of the antenna cannot be approved. This is the reason why in this step of optimization return loss is still one of the main concerns.

The other parameter is the length of the antenna. As the dimensions of

the antenna is one of the requirements in the design, it should be confirmed that the antenna cannot be designed with a shorter length and the same (or higher) performance. The length of the antenna is a summation of the length of different parts in the antenna, indeed. So, if it is going to be reduced, it should be reduced from one or a few of those parts. The radiation flares, in this respect, are not an option due to the fact that many simulations have been done on them and their results show that those are the optimum size for the flares. The MTL, on other side, has 3 parts in which the first 2 parts are too short to influence on the total length considerably (or significantly). Eventually, the linear transition - the 3rd part of the MTL - remains to be shortened. That is the second parameter which has been used in these simulations in addition to the ending impedance, Z_f. The value of this parameter is chosen as $l_m = 2.5\lambda_c$ and $l_m = 3\lambda_c$ where λ_c is the wavelength of the center frequency in the frequency band of $0.1-6$ GHz, $f_c = 3.05$ GHz.

To study the impact of the length of the transmission line on the performance of the antenna fairly, a straight transmission line with the length of the $l_a = 0.5\lambda_c$ has been added to the shorter models. In this way, in all four models the wave propagate on the same length and will be emitted on the same spot more or less.

So, 2 parameters, each with 2 values, make 4 models in combination. To find out the optimum model, the decision has to be made based on 3 criteria:

- Return Loss

  The return loss of the models are depicted in figure 3.22. They all meet the required bandwidth[3], $0.3-6$ GHz, and in this respect there

[3]The models in this section are simulated to $f_{max} = 4.5$ GHz due to lack of computational memory.

is no competition among them. Surely, one might find differences in the graphs of these models. However, these differences such as number of deeps and peaks are not important at this stage as they are all operating in desired frequency range.

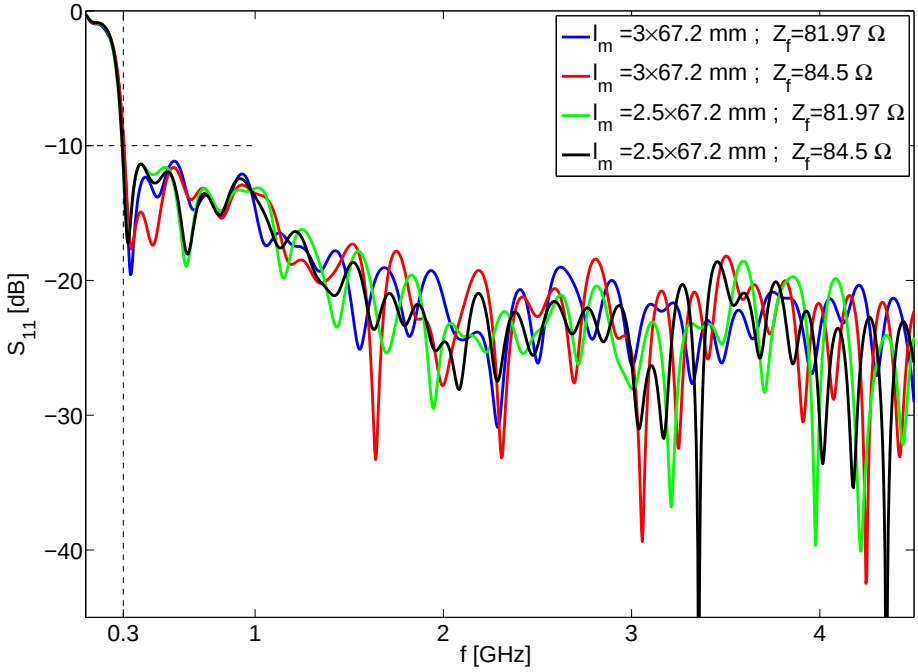

Figure 3.22: Return Loss of the Four Models

- Radiation Characteristics

  To investigate in radiation characteristics, 9 co-polar and 9 cross-polar probes are located 100 cm away from the port location in simulations. The configuration of the probes is illustrated in figure 3.23.

  The captured pulses in these probes, $y_p(t)$, which show the radiated signal in the near field of the antenna, are first transformed to the

Based on the previous results and simulations, these antennas should be investigated in low frequencies of the desired bandwidth where they might show mismatch. So, generality will not be missed by choosing $0.1 - 4.5$ GHz as the simulation bandwidth.

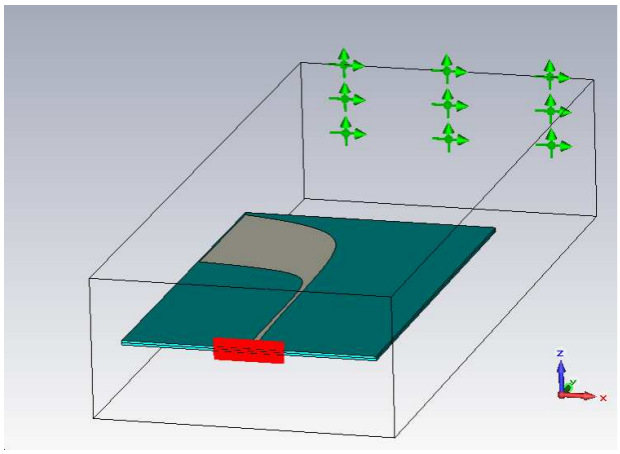

Figure 3.23: Positions and Configurations of the Probes

frequency domain using *fft* function in MATLAB, $Y_p(f)$, and, then, the transfer function, $H(f)$, for each location can be calculated easily by dividing the received pulse at the probe location, $Y_p(f)$, to the main pulse of port in frequency domain, $X(f)$. Using the inverse transform, *ifft*, it can be converted in time domain, $h(t)$. So, it is possible to observe the impulse response in each position and configuration (co-/cross- polarization) in time domain.

The radiated pulse in two positions out of nine are illustrated in figures 3.24. In both figures, the shorter models unexpectedly are performing better. The green and black curves which are corresponding to 81.97 and 84.5 Ω final impedances, respectively, of the shorter models have higher peak-to-peak ratio and lower levels of ringing. The difference is significant enough to go for them due to the fact that these models are supposed to be shorter than the other ones. It should be noted that these models have the same total length for this experiment but the shorter models consists of a straight transmission line which can be removed. By removing those straight lines, these models will be 3.3 cm

shorter.

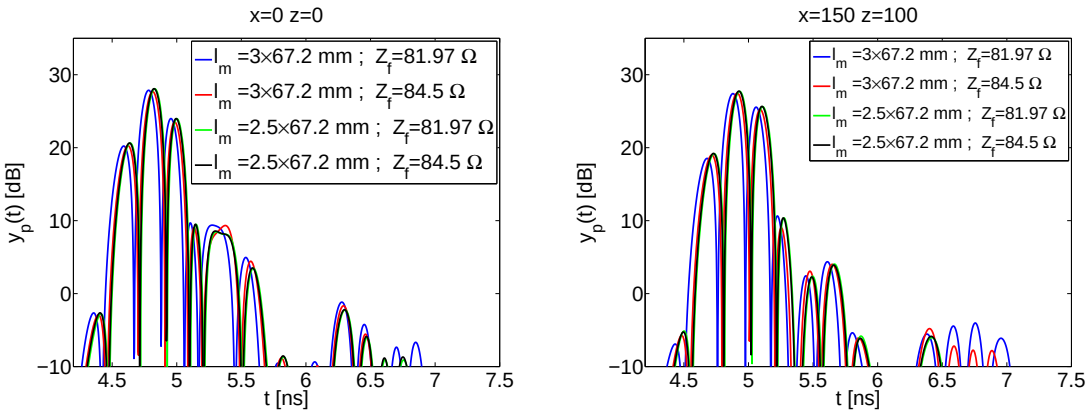

(a) (b)

Figure 3.24: Radiated Pulse of the 4 Models Captured by the Probe located at $(x = 0, z = 0)$ and $(x = 100, z = 150)$ mm

The impulse responses of the antennas in time domain are also illustrated in figure 3.25(a). For this purpose, the probe which is located at $x = 0$ and $z = 0$ mm is taken as the sample. For the same position, the transfer functions of the antennas are illustrated in figure 3.25(b). The radiated pulses are normalized to their maximums so that the impulse responses and transfer functions can be compared fairly. Of course, the objective of this study is not the gain of the antenna as they almost possess the same gain over frequency. It is, actually, the shape of the impulse response to see possible distortions.

From the figure 3.25(b), the graphs are so similar that the comparison is not possible. They have an almost flat frequency response which is lower for low frequency components in the range. This is also reasonable due to the fact that the antenna in low frequencies has lower gain than higher frequencies of this range. Figure 3.25(a) has more infor-

mation, though. In this figure, the blue curve has slightly intensive late-time ringing which is depicted in a box inside the figure. The rest of the models in this respect are performing most-likely the same. Although one might find some minor differences or even better results for the red curve, this difference is negligible considering the optimization of the ending of the flares.

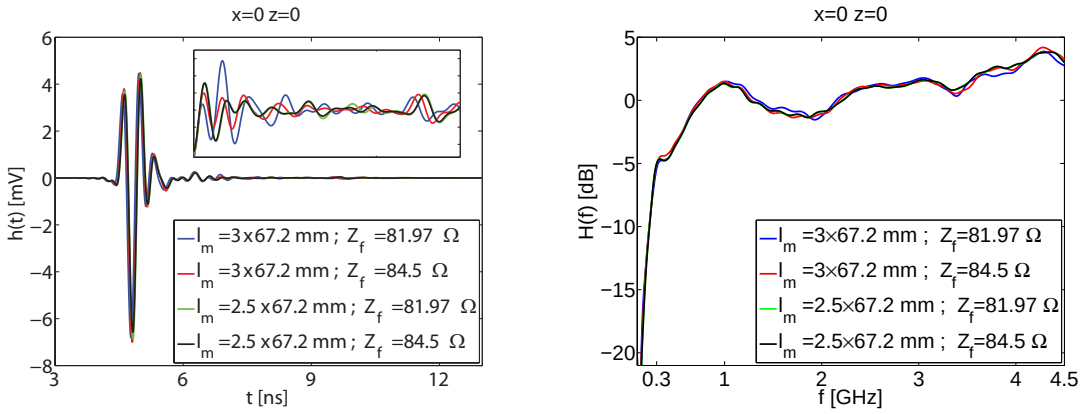

(a) Time-Domain

(b) Frequency-Domain

Figure 3.25: Impulse Response and Transfer Function of the 4 Models Captured by the Probe located at $x = 0$ cm and $z = 0$ cm

- Size

  This element in the design criteria is important due to the lower manufacturing cost of the smaller planar antennas. Obviously the shorter models are better in this sense.

By considering a combination aspects of the models, the optimum design is the one which was depicted in all the figures of the section 3.4 by green curve. This antenna has the final impedance of $Z_f = 81.97\ \Omega$ and the linear transition section is designed with the length of $l_m = 2.5\lambda_c$. As

described earlier, it has a straight transmission line which was supposed to be removed for further designs and that was the main motivation for this antenna. However, when it is removed from the antenna and the flares were attached to the end of the linear transition line with the length of $l_m = 2.5\lambda_c$, the performance degrades. This happens for the other model with this length as well.

So, the red model is substituted with these two models for the rest of the project as it is performing better than the blue model.

Complete BAVA Simulations and Results

4

In the previous chapter, the antenna optimization accomplished. Some of the required features, such as return loss of the antenna, substrate material and matching to 50 Ω impedance has been achieved. This chapter consists of two sections in which the finalizing issues of the antenna are discussed.

In section 4.1, the appropriate SMA end-launch to feed the antenna is reported. This connector is modeled in CST MW Studio and imported onto the models. Thus, the antenna models which are discussed in this chapter are fed by SMA end-launch instead of previously used waveguide port. The simulations, thus, lead to more realistic results.

By adding the SMA end-launch and to finalize the design of the antenna, the ending of the antenna is optimized. The results of this optimization process are explained in section 4.2. Finally, this chapter is concluded with results of the optimum antenna in different aspects of radiation in section 4.3.

4.1 The SMA connector

SMA end-launch connects the planar antennas printed on substrate to coaxial cable so that the excitation impulse can derive it. To solder the SMA end-launch to the antenna, the pin should be soldered anyhow on the middle layer and the outer pins should be soldered to the outer layers. The problem is, however, that the middle layer is hidden between 2 substrate

sheets and the pin cannot be soldered on this layer. This was addressed in chapter 2 for the first time and now a solution has been suggested to make it doable. This solution is explained in section 4.1.1.

Suggesting the operational solution for this problem, the suitable SMA end-launch is found. Then, it is modeled and imported on the rest of the antenna models.

4.1.1 The Hidden Layer Problem and Solutions to Solder the SMA End-launch

The first solution for this problem is to order the antenna in two disjoint sheets (figure 4.1(a)). On one sheet two layers of BAVA are printed and the other layer is printed on the second sheet. The SMA end-launch will be soldered on the sheet which has two layers. Then, the other sheet will be glued to it. This solution is very easy to implement however, there are a few cons which should be considered.

The first disadvantage is that the replacement of the SMA end-launch is impossible for this antenna. Secondly, even though the glue with the same permittivity as the substrate is used, it will change the electrical characteristics by adding an air gap between the layers. And finally, the antenna will be glued manually which increase the human-made errors.

In the second method, a hole will be drilled on the stripline to reach the middle layer from the top (figure 4.1(b)). Then, the SMA end-launch will be connected on top of the antenna such that the pin will touch the middle layer. From one side, its ground is connected to the top layer and it can be extended to reach the bottom layer of the antenna. This approach can solve the replacement problem of the first method but it introduces other

problems in the feeding of the antenna.

One of the problems is the direction of the connection to the antenna which is orthogonal to the traveling direction of the wave on the antenna. This may cause strong reflection to the feeding which is not convenient for the antenna. Another problem is the difficulty of soldering the pin to the middle layer.

To solve the aforementioned problems of previous approaches, the third method is suggested. In this method, a cubic volume is taken from the upper sheet of the antenna (figure 4.1(c)) so that the middle layer appears. The pin can now be connected to the middle layer, it can be easily replaced and the wave starts the journey on the antenna with the same direction it has come from.

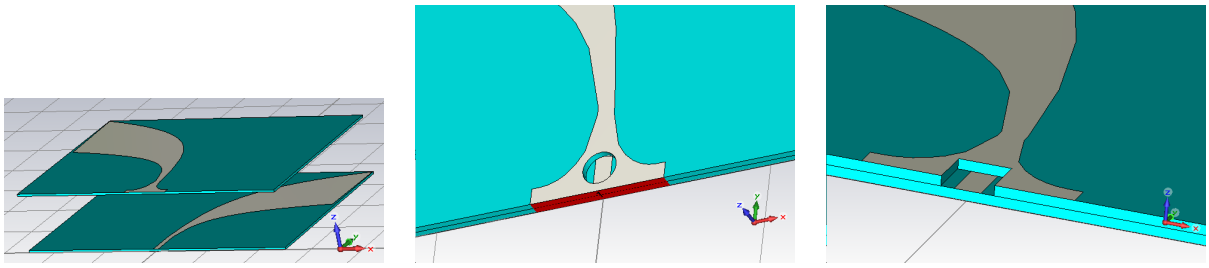

(a) Solution One (b) Solution Two (c) Solution Three

Figure 4.1: Proposed Solutions for Soldering the SMA end-launch to the Antenna

4.1.2 Finding a Suitable Connector

Hopefully, based on the proposed solution in section 4.1.1 many conventional SMA end-launches can be used. To find a suitable connector for the designed antenna among the RF/Microwave connectors, the catalogue of the "Emerson Network Power Connectivity Solution" is studied. The main

concerns to find the connector are: dimensions, operation frequency and input impedance.

With respect to the dimensions, the connector should be plugged to the antenna in such a way that its central pin soldered to the middle layer and its holder box should be large enough to be soldered to the outer layers, both on top and bottom. Since the inner layer of the antenna is 5 mm wide, the connector's outer radius should be larger to avoid any contact between these layers. Hence, the outer diameter of the dielectric cylinder of the SMA should be higher than 5 mm.

Another aspect apart from the dimensions is the operating frequency of the SMA end-launch which should support the range of $0.3 - 6$ GHz. Moreover, the input impedance of the connector should be 50 Ω to match the antenna and the output of the pulse generator.

Based on these requirements, two connectors are chosen. These are both SMA end launch jack connectors, except that the type of contact (pin) differs[1]. Hereby, brief and important specifications of them are reported as well as the figure of the one with round contact [2] (figure 4.2).

Figure 4.2 shows the SMA end launch which is best suited in our purpose. The operating frequency of this connector is $0 - 18$ GHz which covers the range of our designed antenna. In this range the VSWR of the connector is said to be below 1.5 for the 50 Ω impedance. The isolator of this SMA end launch is a type of Teflon. To use this connector, however, the four legs should be cut. Thus, the entire width of the connector can be used in order to solder it on the outer layers of the antenna.

[1]For a full description of the connector, the reader is referred to page 54 of the catalogue.

[2]The other one has a "tab" contact

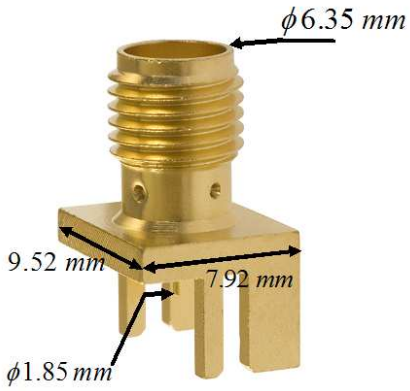

Figure 4.2: 50 Ω SMA End Launch Jack Receptable - Round Contact

4.1.3 Simulations of the Connector

In the first step the connector is simulated in the CST to check the input impedance, separately. The input impedance based on the simulation results for the connector without the legs is 49.98 Ω. This is the impedance in the central frequency (3.05 GHZ for this simulation) and might change little over different frequencies, but the variation is negligible. Also, the permittivity of the insulator might be different from the original connector. Although these details will not change the final result of the work, it is better to keep them the same as the original connector. This issue, to the author's best understanding, is considered in the entire simulation process.

Afterwards, the simulated connector is imported to the main simulation of the antenna and connected to it. Figure 4.3 shows the way that the connector has been connected to the antenna.

The return loss of the antenna which is excited through the SMA end-launch does not vary in low frequencies of the range. The variation in return loss occurs in high frequencies, but the S_{11} remains below -10 dB which is the acceptable threshold. The results of this simulation is not shown here, because it is included in the rest of the work which is presented with more

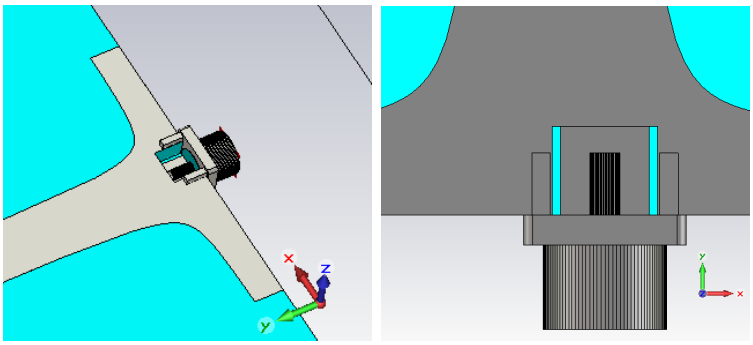

(a) (b)

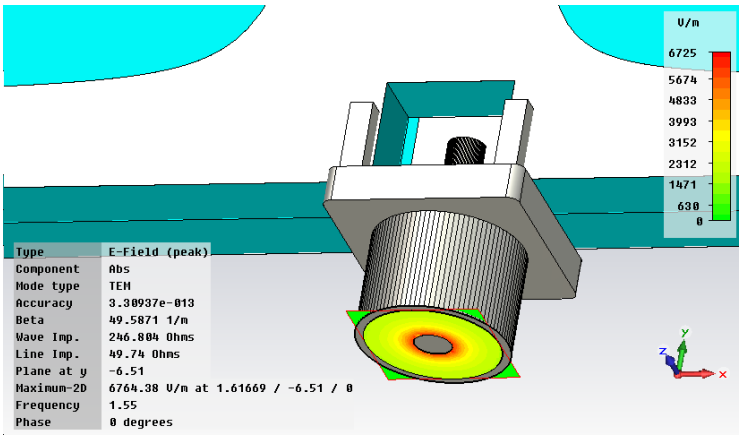

(c)

Figure 4.3: Simulated SMA End Launch Connected to the Antenna

details later in this chapter.

4.2 Optimization of the Antenna Ending

The main radiation in the antenna occurs in the starting opening of the flares. This can be approved by observing the surface currents on the antenna flares. After the main radiation, whatever happens to the pulse on the antenna causes late time radiation phenomenon.

From previous simulations, it has been observed that a strong reflection occurs when the pulse reaches the straight structure at the end of the flares, ending of the antenna. This strong reflection bounces between the opening of the flares or feeding and the ending of the antenna and causes multiple reflections and radiations. To avoid this fatal impact of the straight ending, it should be modified so that the reflection at the ending does not occur or at least alleviated.

To do so, 2 endings are proposed in 2 recent works, separately. In [12], the corrugated ending is added to the antenna in order to kill the backwards currents in that region. The idea is implemented on the coplanar Vivaldi antenna, but the results of their work does not show any significant improvement. Due to the fact that the corrugated ending is expected to work based on acceptable physical assumptions, it is still one the suggested methods and has been applied to the ending of the designed BAVA (figure 4.4(a)). In the second approach, a circular or semi-circular ending is applied to BAVA (figure 4.4(b)), [13], [35]. These approaches are addressed with *corrugated* and *bent* in following results, respectively.

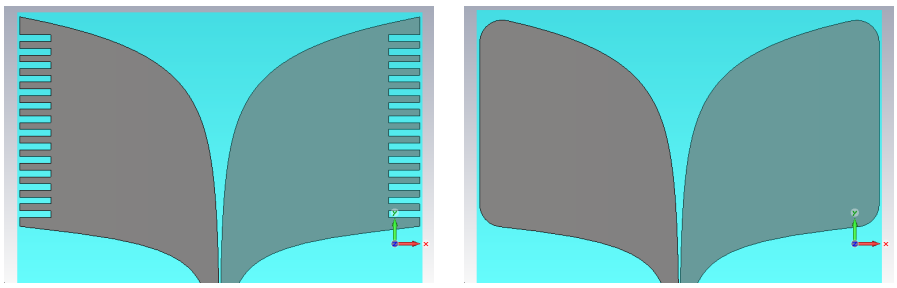

(a) Corrugated (b) Bent

Figure 4.4: Simulated Endings of BAVA

Investigation on corrugated ending shows that it is not a suitable ending

for the antenna. The operating frequency band of the antenna is decreased and the matching margin of the return loss in lower frequencies is gone. This can be seen in figure 4.5(a).

Also, the radiated signal is collected by a probe which is located 100 cm away from the port in both simulations. This sample does not show the entire radiation but it is enough to check if the antenna is capable of emitting a suitable pulse. The result is illustrated in figure 4.5(b). Both pulses are normalized to their maximums and are illustrated in dB scale. The main pulses for both endings have the same shape however the ringing of the corrugated ending is increased. This increment can be seen in 2 aspects: first, the level is increased and, secondly, the number of pulses after the main pulse is increased. This experiment shows that the corrugation is not a suitable method for ending BAVA.

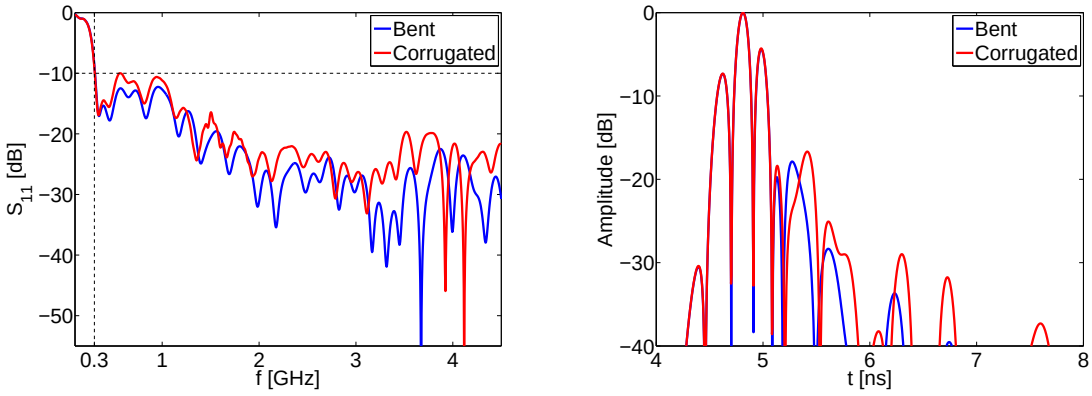

(a) Return Loss

(b) Normalized Radiated Impulse at $(x = 0, z = 0)$ 1 m away from the probe

Figure 4.5: Comparison of Bent and Corrugated Ending on Return Loss and Radiated Near-Field Impulse

The only option left is to bend the ending of the antenna. The bending

can be done by various radii for each curve. In other words, the inner curve at the ending can be bent with R_i which is different from R_o, the radius of bending for outer curves. Therefore, 3 radii has been chosen for each of the inner and outer curves. The maximum radius is 82.8 mm by which a circle can be drawn inside the opening of the flares. 20 and 50 mm are also chosen as 2 radii for this experiment. In total, 9 models can be made. These models are exactly the same as the optimized model of section 3.4 except the ending which is modified in this section.

To compare these models, 3 criterion are considered: return loss, radiated pulse 1 m away from the antenna at $(x = 0, z = 0)$ and the far-field pattern. The last criterion is used to see the amount of back-radiation of the antenna. It is, actually, anticipated that the higher radius for the curves might cause back- and side- radiation as the currents are flowing on that part of the antenna. One of the ways to test the correctness of this expectation is to see the far-field pattern of the antenna. Checking the current distribution is also helpful, but it does not prove anything. Of course, it would be more convenient to check the radiation of the antenna at side and back of it, but available computational memory does allow to go over a certain volume.

The antenna with radius of $R_i = 20$ and $R_o = 20$ mm shows the best results among the other models. This model, in fact, has the maximum operating frequency and lowest back-radiation level. The main pulse is almost the same for all models, but the ringing is reduced significantly in this model. The comparison results of this section might distract the readers. So, it is reported in appendix A. The geometry of this model is delineated in figure 4.6.

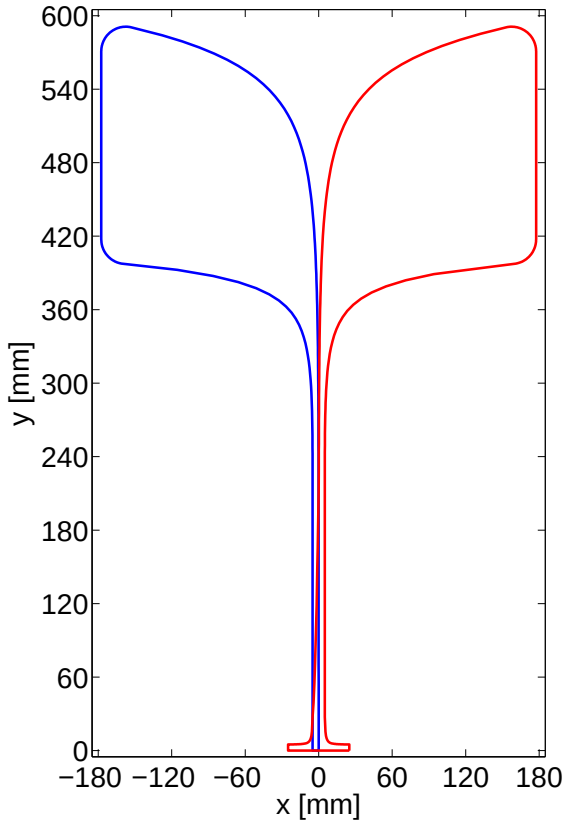

Figure 4.6: Geometry of the Optimum Model

4.3 Radiation Characteristics of the Optimum Antenna

In this section the results of the simulation on the optimized antenna is presented. The results are over various aspects of the radiation in UWB and antenna characteristics. These characteristics are considered and studied in both time and frequency domains. As mentioned earlier, the antenna in this section is fed by a SMA end-launch which makes the results more reliable and real.

The first characteristics of the antenna is the return loss (figure 4.7). This

graph shows that the antenna is matched to the feeding line and has a number of internal reflections to the feeding. This can be figured out from the frequent deeps of the in higher frequencies of the range. Based on the definition of the operational frequency bandwidth, this antenna starts to work from $f = 304$ MHz. In higher frequencies of the range it shows a reliable +10 dB margin. The highest frequency, due to the lack of computational power, is $f = 4.5$ GHz. Higher frequencies leads to astonishing number of mesh cells in the simulation. Simulations without SMA end launch appears that the antenna is operating to 6 GHz.

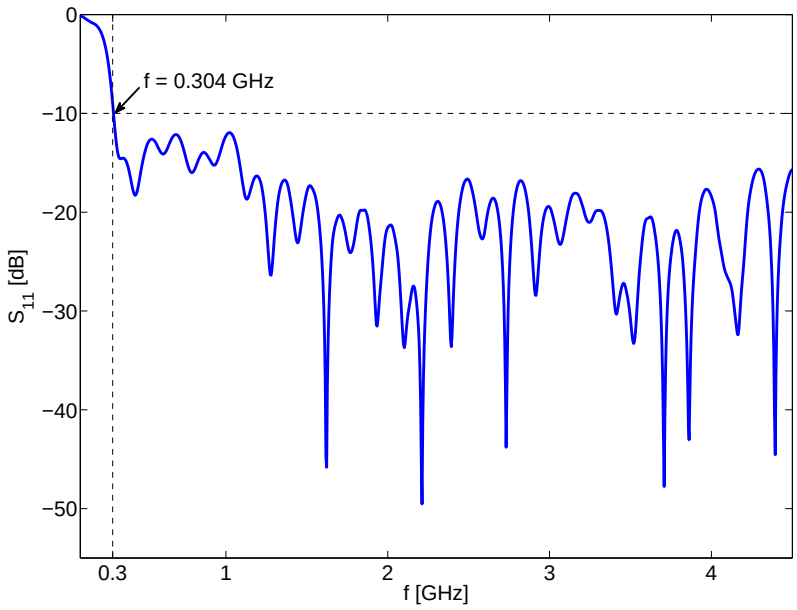

Figure 4.7: The Return Loss of the Optimized Antenna, Matched with a SMA End-launch Connector to 50 Ω

Another feature of the antenna is its far-field pattern. For this antenna, the far-field pattern is sampled at $f = 0.3$, $f = 1.5$, $f = 3.05$ and $f = 4.4$ GHz and illustrated in figure 4.8. In lowest frequency of the range, $f = 0.3$ GHz, the antenna operates very similar to a half-wave dipole. In

higher frequencies the antenna inherits the directional characteristics of the Vivaldi antenna. Back- and side-radiation of the antenna is almost 20 dB less than the radiation in the end-fire direction in these frequencies. Stable pattern, flat gain and wide beam-width are the characteristics which can be named for this antenna.

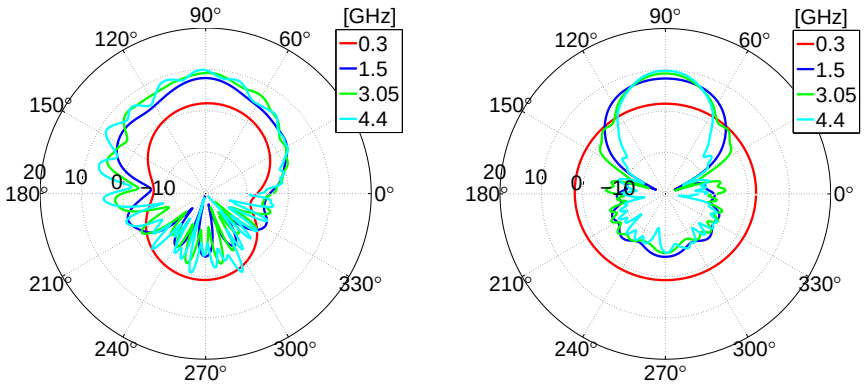

(a) E-plane

(b) H-plane

Figure 4.8: The Far-field Gain Pattern of the Antenna at $f = 0.3$, $f = 1.5$, $f = 3.05$ and $f = 4.4$ GHz in E- and H-plane

After far field pattern of the antenna, the foot-print of the antenna can be discussed. To find the foot-print of the antenna, an area of 1 m $\times$ 0.5 m is covered by probes in both co and cross polar configurations. Each probe captures the radiated pulse in that position in the entire experiment and thus the peak-to-peak value of the pulse can be obtained easily. It can be used directly to show the area where the antenna can illuminate. However, the ratio of the peak-to-peak value of the co-polar probes to the correspondence cross-polar probes is calculated and the result is depicted in figure 4.9. Vertical axis in this figure shows the $z-$axis while horizontal axis is mapped to the $x-$axis. The antenna is laid, just like before, on the

$xy-$plane and the plane of these probes are 30 cm away from the ending edge of the antenna. The figure is scaled in dB. This means that if a certain point is colored with corresponding color with 20 dB, at that point the cross-polar electrical field is 20 dB less that the co-polar field.

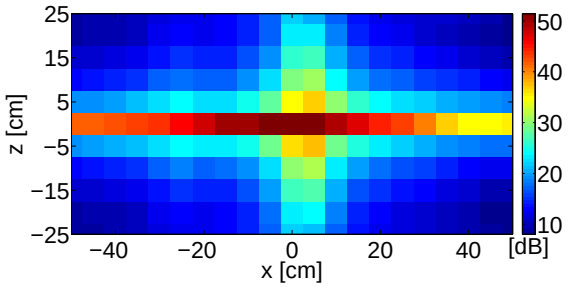

Figure 4.9: Co-polar to Cross-polar Ratio of the peak-to-peak levels of the main pulse

Considering the 20 dB co-polar to cross-polar ratio as the threshold for the performance of the antenna, a circular area of 1 m^2 can be determined as the illumination area of the antenna. The peak-to-peak level of co-polar probes is depicted in appendix A. This figure, in contrary to figure 4.9, shows that the entire area is illuminated by high peak-to-peak level. So, if the cross-polar radiation was not an issue for the detection or application of the system, the entire 1.5 m^2 would have been determined as the illumination area.

The radiated pulse at some of these probes are demonstrated in figure 4.10. In this figure, to have a better view, the pulses are shifted such that the main pulse of them occurs in the same time. Although this time is not real, the whole figure can be better observed.

Figure 4.10(a) shows a high-correlated pulse with a small ringing. The amplitude of the pulses are degraded when they are taken from outer locations of the foot print area. Figure 4.10(b) confirms the small ringing of

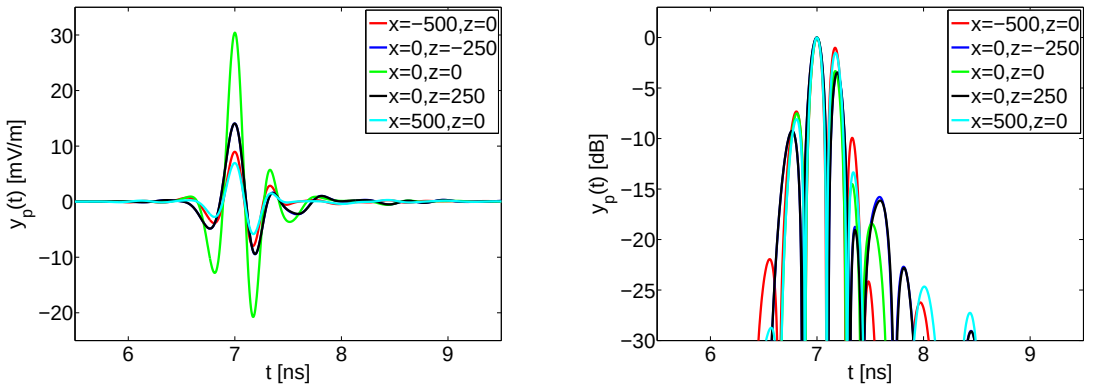

(a) Linear Scaling

(b) Normalized and Logarithmic Scaling

Figure 4.10: The Radiated Pulse, Captured By the Probes in Different Locations

the radiated pulses. In this figure, the pulses are normalized and shifted to the same time. The ringing is 20 dB less than the main pulse which is an important characteristic of the antenna.

To see the correlation between the excitation and radiated pulses on the ground, the fidelity factor can be used. This is a proof which shows how much the radiated pulses are similar in shape to the excitation pulse and of course to each other. The fidelity factor for this antenna has been calculated and depicted in figure 4.11. This has been done for the first derivative of the excitation pulse as the antennas with flat gains ideally radiate the first derivative of the excitation pulse.

This factor is normalized, thus, the overall amplitude of the pulse does not impact on it. The figure shows that the fidelity is high enough (more than 0.95) for a reasonable area and will be degraded in the upper and lower z. This means that the antenna can illuminate the ground with the same pulse over a large area which could be expected based on the gain pattern.

Another approach to illustrate the radiation characteristics of the an-

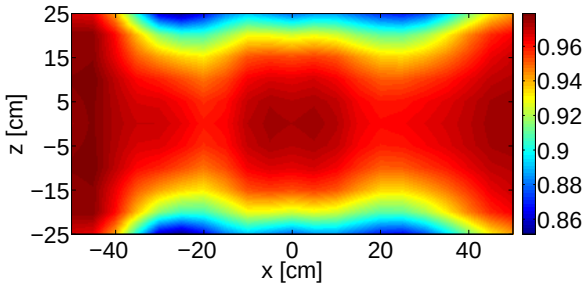

Figure 4.11: Fidelity Factor between the First Derivative of the Excitation Pulse and Radiated Pulses on the Foot-print Area

tenna is the B-scan. B-scan can be attained in E- and H-planes of the antenna. This has been done and the result is demonstrated in figure 4.12. The pulses in this figure are normalized and depicted in logarithmic scale, dB. In this figure, the pulses less than −25 dB are not depicted. Thus, the figure clearly shows that the antenna radiate very small late time ringing if any.

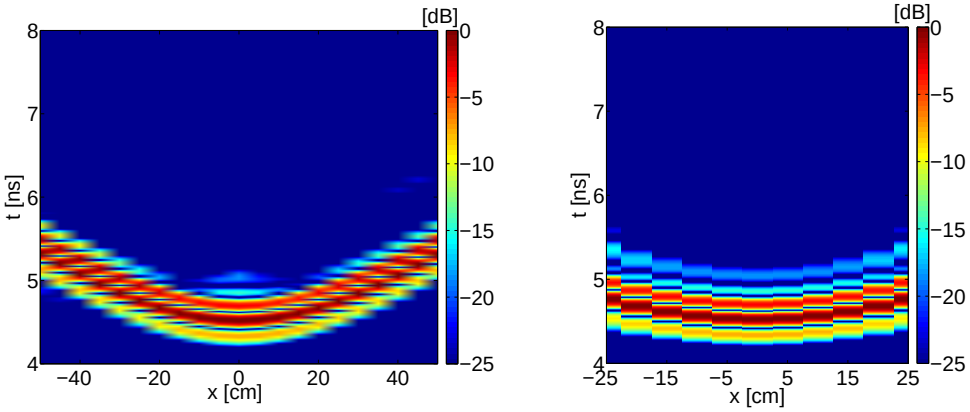

(a) E-plane

(b) H-plane

Figure 4.12: B-scan of the Captured Pulses in E- and H-palnes

The transfer function of the antenna is calculated by dividing the Fourier transform of the captured pulses to the excitation pulse. In this way, the

excitation pulse is excluded from the radiated pulse and the transfer function can be calculated. This calculation has been done for the same probes are the previous ones and the results are demonstrated in figure 4.13. This figure shows that the antenna has a flat gain over a wide frequency band. In lower frequencies, however, a variation in the magnitude of the transfer function can be seen. This happened not in the center of the area but in the far end of the area. It should improve for the further works on this project.

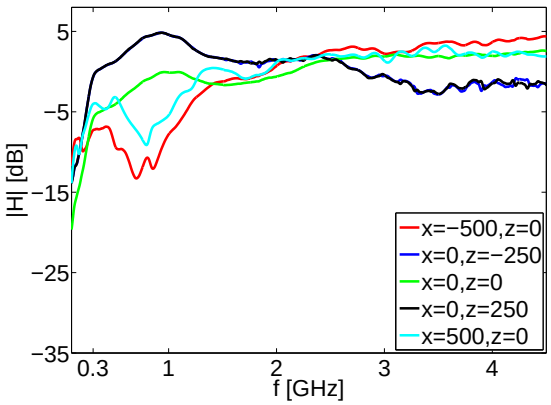

Figure 4.13: Transfer Function in dB Scaling at Different Probe Positions

The impulse response is calculated by taking the *ifft* of the transfer function. They are shown in figure 4.14 in linear and dB scales. In this figure, the main impulse is shifted to the same position in time. The impulse response in figure 4.14(b) confirms that the late-time ringing of the antenna is less than -20 dB. Both figures illustrate the capability of radiating a narrow-band pulse.

Finally, the radiation group delay of the antenna for one probe as a sample is derived from the transfer function of the antenna at that position and depicted in figure 4.15. The group delay in this figure confirms another capability of the antenna to keep the radiated pulse non-distorted. The

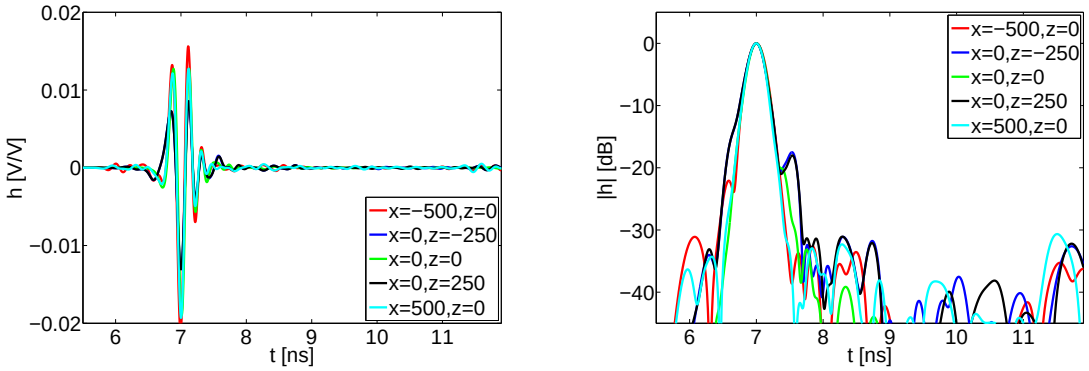

(a) Linear Scale

(b) Logarithmic Scale

Figure 4.14: Impulse Response of the Antenna in Different Locations of the Foot-print Area

group delay of the antenna after $f = 0.3$ GHz can be fitted in a range about $\delta\tau = 0.3$ ns which is a reasonable value for a broadband antenna.

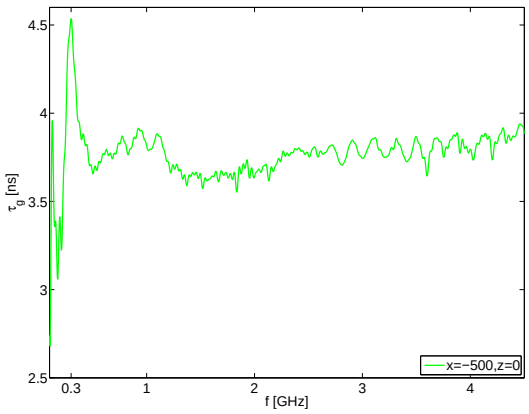

Figure 4.15: Group Delay of the Radiated Pulse Towards the Central Probe

From the aforementioned results, the optimized antenna shows the required capabilities of the desired design of the project. Of course, the room for improvement is still available in order to increase the illuminating area. Also, the back-radiation of the antenna is still severe and should be im-

proved.

Conclusions, Recommendations and Final Remarks

5

5.1 Conclusions

In this project, an UWB antenna for GPR application is designed and simulated. Various UWB antennas are studied in order to find the most suitable family of antennas for the purpose of the project. Promising performance of the designed Vivaldi antennas in the last few years triggered the investigation on this type of antenna for this project.

Various types of the Vivaldi antenna are studied in-detail and, finally, an extensive research over their capabilities, advantages and disadvantages are carried out by means of CST Microwave Studio simulator software. The results of the simulations in the early stage provided a bright overview of the characteristics of the various types of Vivaldi antenna. They, also, guided the project to take the balanced antipodal Vivaldi antenna (BAVA) as the main candidate.

Optimization on different parts of the BAVA is done. The simple optimization process for this project, although converged to the final solution, faced with many challenges. The first one was the design of the flares with respect to the dimensions and curvature of the flares. This challenge has been solved by creating over 100 simulations, but then, another challenge came through. The most difficult and common challenge of many recent BAVA antennas. It is found for the first time and called "the transition disaster" which is addressed in 3. A novel and successful solution for this

challenge is suggested. The solution, although very simple, can resolve the returned pulse from the transition of the transmission line to the flares and improve the performance of the antenna.

The same optimization approach is taken to design the where the transmission line of the antenna. The transmission line is optimized based on the smoothest and shortest architecture for the line. The radiation characteristics of the antenna is verified when the flares were connected to the transmission line. The matching to 50 Ω input impedance of the antenna is confirmed by many simulations over the entire frequency band.

To complete the design of the antenna a SMA end-launch is added to the structure of the antenna. The simulations with the end-launch showed that the stripline is one the most stable structures in this respect. The entire antenna then simulated and its radiation characteristics are investigated.

Finally, from the obtained results, it is approved that the designed antenna has an overall acceptable performance. It has constant group delay, stable and flat transfer function, narrow width impulse response with small late time ringing and acceptable illuminating foot-print.

5.2 Recommendations, Remarks and Future Works

The antenna, as discussed in chapter 4, meets the requirements of this project, but it is not the ideal antenna with extraordinary features. Actually, the room for improving this antenna is still available on different aspects. Among them, increasing the illumination area seems to be the most important one. This can be done by changing the ending of the antenna and, of course, is a comprise among other features. For example, by increasing the radius of the bending of the inner flare, the illuminating area

might increase. However, the radiated pulses will not be radiated from the same spot on the antenna. Moreover, it may introduce higher level side-lobes in the pattern of the antenna. Thus, the optimization process should be carefully applied to handle this trade-off with the satisfactory result.

The corrugated ending was shown as the unsuccessful approach. However, it has many parameters to be tuned and also it is coming from a correct Physical assumption. So, it is suggested to continue with this antenna and a corrugated ending.

In an more general view, the optimization approach should be improved. A mature optimization approach, such as fuzzy logic approach, with enough theoretical background, both in antenna design and in optimization process can be used to solve the problem much faster and more accurate.

Apart from that, The design process in this Thesis was based on previous works and without solid theoretical models. So, for the next step, it might be interesting to design an antenna based on a pure theoretical optimization. In other words, it can be the optimization based on the Green functions of the antenna.

Finally, the designing process of an antenna is found analogous to solving a broken puzzle. The pieces of this puzzle are available and the frame is also defined. Thus, the designer should take the right pieces wisely and put them in their positions. Otherwise, this puzzle will be a job for the rest of his/her life.

Nine Models of the Ending

A

In the chapter, the results of the simulations on the 9 models of the section 4.2 are compared. Comparing the obtained results, the optimum design is chosen among them.

The back- and side radiation is the main side effect of adding curvature to the ending of the antenna although this may help emitting better pulses. Therefore, in this experiment, first the pattern of the models are considered. The gain of the models are depicted in figure A.1. Models are grouped in 3 subsets. Each subset has the models with the same inner radius. Each sub-figure in figure A.1 shows the gain of the models in each set. From each set, the model with the lowest back-radiation is taken for the next round of comparison. The best models in each subset should possess the lowest back- and side radiation gain. Based on this criteria, the following models are chosen: $(R_i = 82.8 \text{ mm} - \text{R}_\text{o} = 20 \text{ mm})$, $(R_i = 50 \text{ mm} - \text{R}_\text{o} = 20 \text{ mm})$ and $(R_i = 20 \text{ mm} - \text{R}_\text{o} = 20 \text{ mm})$.

In the next round, radiated pulse of the 3 models are compared in figure A.2. This figure shows that the green graph has higher peak-to-peak level and lower late-time ringing. So, this model is picked as the optimum model among these nine models for the project.

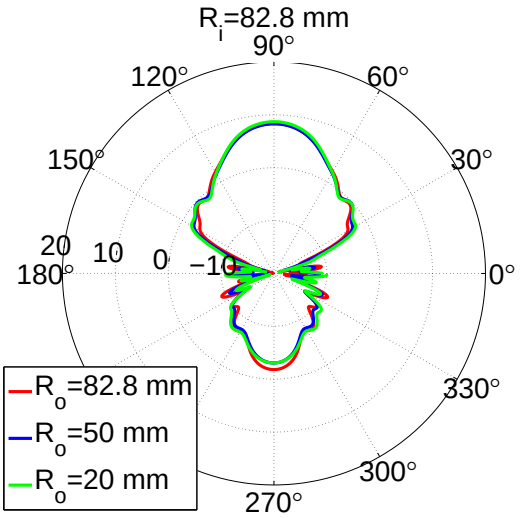

(a) $R_i = 82.8$ mm

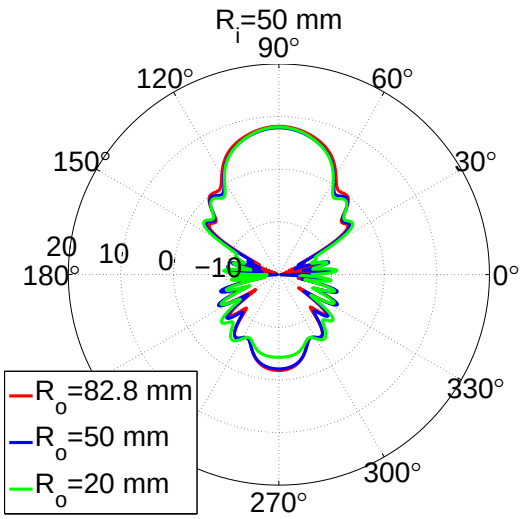

(b) $R_i = 50$ mm

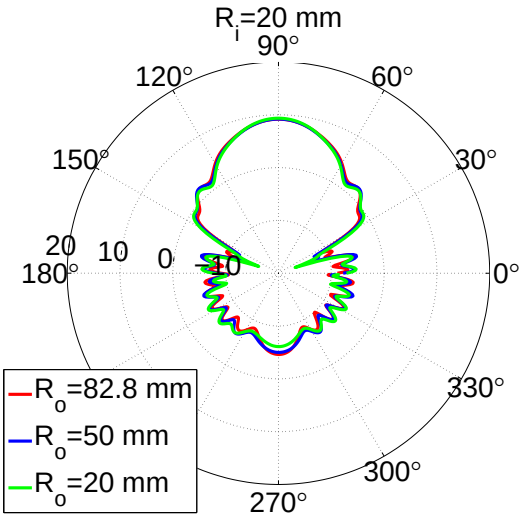

(c) $R_i = 20$ mm

Figure A.1: The H-plane Gain of the 9 Models

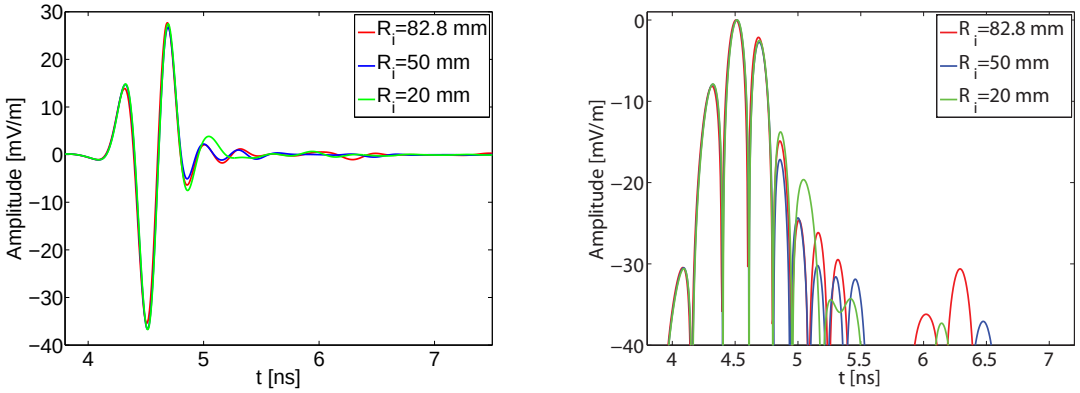

(a) Linear Scaling

(b) Logarithmic Scaling

Figure A.2: Radiated Pulse of the 3 Models, Captured in the Central Probe

More Results of Optimum Antenna

B

Two figures are shown here to complete the obtained results of the optimum antenna. In figure B.1, the feeding section is depicted. The input impedance of the antenna is also mentioned in figure which is 50.1 Ω. The impedance of this structure varies with the number of pieces which are used to create the cylindrical shape of the feeding. Using more pieces increases the accuracy, but also computational time and memory. So, the number of pieces in this simulation is moderated in order to decrease the required computational power.

Figure B.2 demonstrates the foot-print of the main radiated pulse. Both sub-figures are scaled in dB in order to have better view.

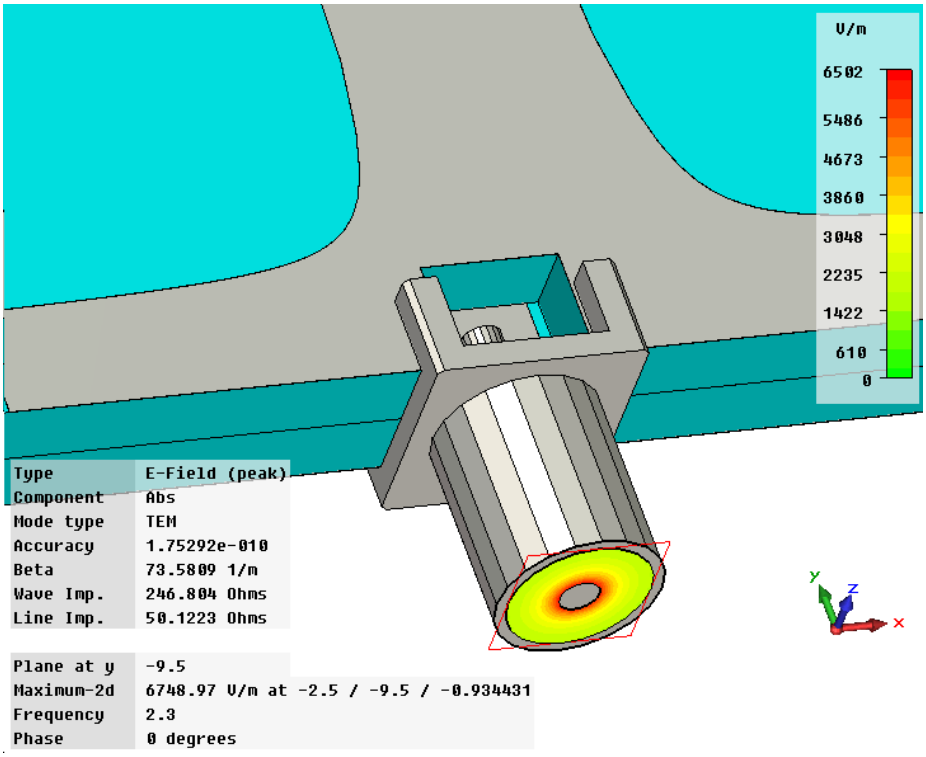

Figure B.1: Excitation of the Optimum Antenna via SMA End-launch

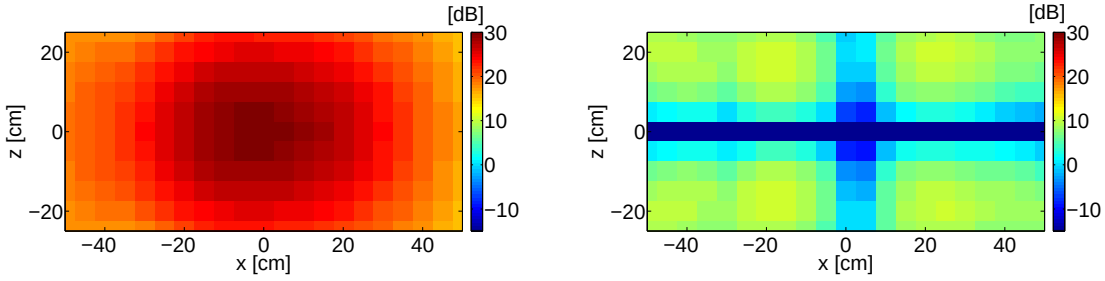

(a) Co-polar Probes

(b) Cross-polar Probes

Figure B.2: Foot-print of the Peak-to-peak levels of the Main Radiated Pulse

Bibliography

[1] W. L. Barrow and L. Chu, "Theory of electromagnetic horn," in *Proceedings of IRE*, vol. 27, pp. 51–64, January 1939.

[2] D. J. Daniels, *Ground Penetrating Radar*. Institute of Engineering and Technology, 2nd ed., 2007.

[3] A. Yarovoy, "Adaptive bow-tie antenna for ground penetrating radar," in *Tenth International Conference on Ground Penetrating Radar*, pp. 121–124, June 2004.

[4] A. A. Lestari, A. G. Yarovoy, and L. P.Ligthart, "*RC*-loaded bow-tie antenna for improved pulse radiation," *IEEE Transactions on Antennas and Propagation*, vol. 52, pp. 2555–2563, October 2004.

[5] A. G. Yarovoy, A. D. Schukin, I. V. Kaploun, and L. P. Ligthart, "The dielectric wedge antenna," *IEEE Transaction on Antennas and Propagation*, vol. 50, pp. 1460–1472, October 2002.

[6] D. Caratelli, H. Poley, and A. Yarovoy, "Em characterization of resistively loaded printed dipole antennas for gpr applications," in *13th International Conference on Ground Penetrating Radar*, pp. 1–6, August 2010.

[7] K. Kim and W. R. Scott, "Design of a resistively loaded vee dipole for ultrawide-band ground-penetrating radar applications," *IEEE Transactions on Antennas and Propagation*, vol. 53, pp. 2525–2532, August 2005.

[8] A. A. Lestari, A. G. Yarovoy, and L. P. Ligthart, "Adaptive wire bow-tie antenna for gpr applications," *IEEE Transactions on Antennas and Propagation*, vol. 53, pp. 1745–1754, May 2005.

[9] A. Z. Hood, T. Karacolak, and E. Topsakal, "A small antipodal vivaldi antenna for ultrawide-band applications," *IEEE Antennas and Wireless Propagation Letters*, vol. 7, pp. 656–660, 2008.

[10] J. Bourqui, M. Okoniewski, and E. C. Fear, "Balanced antipodal vivaldi antenna for breast cancer detection," in *2nd European Conference on Antennas and Propagation*, EuCAP 2007, pp. 1–5, 2007.

[11] A. A. Abbosh, "Directive antenna for ultrawideband medical imaging systems," *International Journal of Antennas and Propagation*, vol. 2008, 2008.

[12] Y. Maksimovitch, V. Mikhnev, and P. Vainikianen, "Characterization of tapered-slot antenna designs for subsurface radar applications," in *3rd European Conference on Antennas and Propagation*, EuCAP 2009, pp. 2811–2813, 2009.

[13] X. Zhuge, A. Yarovoy, and L. P. Ligthart, "Circularly tapered antipodal vivaldi antenna for array-based ultra-wideband near-field imaging," in *6th European Radar Conference*, EuMA 2009, pp. 250–253, 2009.

[14] X. Li, S. C. Hagness, M. K. Choi, and D. W. van der Weide, "Numerical and experimental investigation of an ultrawideband ridged pyramidal horn antenna with curved launching plane for pulse radiation," *IEEE Antennas and Wireless Propagation Letters*, vol. 2, pp. 259–262, 2003.

[15] A. S. Turk, D. A. Sahinkaya, M. Sezgin, and H. Nazli, "Investigation of convenient antenna designs for ultra-wide band gpr systems," in *IEEE Mediterranean Electrotechnical Conference*, MELECON 2006, pp. 557–560, 2006.

[16] A. A. Lestari, A. G. Yarovoy, L. P. Ligthart, and E. T. Rahardjo, "A uwb antenna for impulse radio," in *IEEE 63rd Vehicular Technology Conference*, VTC 2006, pp. 2630–2634, Spring 2006.

[17] A. A. Lestari and et al, "Compact uwb radiator for short-range gpr applications," in *Tenth International Conference on Ground Penetrating Radar*, pp. 1–4, June 2004.

[18] A. A. Lestari and et al, "Design and realization of a gpr antenna for hydrological application," in *11th International Conference on Ground Penetrating Radar*, June 2006.

[19] W. Wiesbeck, G. Adamiuk, and C. Strum, "Basic properties and design principles of uwb antennas," *Proceedings of the IEEE*, vol. 97, pp. 372–385, February 2009.

[20] K. Y. Yazdandoost, H. Zhang, and R. Kohno, "Ultra-wideband antenna and pulse waveform for uwb applications," in *6th International Conference on ITS Telecommunications*, pp. 345–348, January 2006.

[21] C. C. Balanis, *Antenna Theory, Analysis and Design.* John Wiley and Sons, 3rd ed., 2005.

[22] J. Zhao, T. Peng, C.-C. Chen, and J. Volakis, "Low-profile ultra-wideband inverted-hat monopole antenna for 50 MHz 2GHz operation," *Electronic Letters*, vol. 45, no. 3, pp. 142–144, 2009.

[23] I. Hertl and M. Strycek, "Uwb antennas for ground penetrating radar application," in *19th International Conference on Applied Electromagnetics and Communications*, ICECom 2007, pp. 1–4, 2007.

[24] S. Licul, J. A. N. Noronha, W. A. Davis, D. G. Sweeney, C. R. Anderson, and T. M. Bielawa, "A parametric study of time-domain characteristics of possible uwb antenna architectures," in *IEEE 58th Vehicular Technology Conference*, VTC 2003, pp. 3110–3114, 2003.

[25] R. Bawer and J. Wolfe, "The spiral antenna," vol. 8, pp. 84 – 95, Mar. 1960.

[26] P. J. Gibson, "The vivaldi aerial," in *9th European Microwave Conference*, pp. 101–105, 1979.

[27] E. Gazit, "Improved design of the vivaldi antenna," *Proceedings of Institute of Electrical Engineering*, vol. 135, no. 2, pp. 89–92, 1988.

[28] J. Langley, P. Hall, and P. Newham, "Novel ultrawide-bandwidth vivaldi antenna with low crosspolarisation," *Electronics Letters*, vol. 29, no. 23, pp. 2004–2005, 1993.

[29] M. Chiappe and G. L. Gragnani, "Vivaldi antennas for microwave imaging: Theoretical analysis and design considerations," *IEEE Transactions on Instrumentation and Measurement*, vol. 55, pp. 1885–1891, December 2006.

[30] P. Cerny, J. Nevrly, and M. Mazanek, "Optimization of tapered slot vivaldi antenna for uwb application," in *19th International Conference on Applied Electromagnetics and Communications*, ICECom 2007, pp. 1–4, 2007.

[31] E. D. Lera, E. Garcia, E. Rajo, and D. Segovia, "A coplanar vivaldi antenna with wide band balun proposed for the low frequency band of the ska: Approach to the fpa solution," in *IEEE Mediterranean Electrotechnical Conference*, MELECON 2006, pp. 557–560, 2006.

[32] S. Licul and W. A. Davis, "Unified frequency and time-domain antenna modeling and characterization," *IEEE Transactions on Antennas and Propagation*, vol. 53, pp. 2882–2888, September 2005.

[33] D. Cavallo, "An investigation of the performances of ultra wide band tapered slot antennas and arrays," Master's thesis, University of Sannio, 2007.

[34] W. Geyi, "Physical limitations of antenna," *IEEE Transactions on Antennas and Propagation*, vol. 51, pp. 2116–2123, August 2003.

[35] Z. Zhaofa, F. Guangyou, M. F. B. Kamarudin, and M. Sato, "Analysis of balanced antipodal vivaldi antenna and its application for mine-like targets detection," *IEIC Technical Reports*, vol. 102, no. 48, pp. 13–18, 2002.

[36] F. Guangyou, "New design of the antipodal vivaldi antenna for a gpr system," *Microwave and Optical Technology Letters*, vol. 44, no. 2, pp. 136–139, 2004.

[37] E. Guillanton, J. Dauvignac, C. Pichot, and J. Cashman, "A new design tapered slot antenna for ultra-wideband applications," *Microwave and Optical Technology Letters*, vol. 19, no. 4, pp. 286–289, 1998.

[38] J. P. Mahon and R. S. Elliot, "Tapered transmission lines with a con-

trolled response," *IEEE Transaction on Microwave Theory and Techniques*, vol. 38, no. 10, pp. 1415–1420, 1990.

[39] D. M. Pozar, *Microwave Engineering*. John Wiley and Sons, 3rd ed., 2005.

[40] E. J. Park, "An efficient synthesis technique of tapered transmission line with loss and dispersion," *IEEE Transaction on Microwave Theory and Techniques*, vol. 44, no. 3, pp. 462–465, 1996.

[41] M. Vincente-Lozano, F. Ares-Pena, and E. Moreno-Piquero, "Synthesis of tapered transition lines with characteristic impedance optimization," *Microwave and Optical Technology Letters*, vol. 24, no. 4, pp. 277–281, 2000.